Electronic Supplementary Material (ESI) for Journal of Materials Chemistry C.

SUPPORTING INFORMATION

The Fluorination Effect: Importance of Backbone Planarity in Achieving High Performance Ambipolar Field Effect Transistors

Sergio Gámez-Valenzuela,[a] Marc Comí,[b] Sandra Rodríguez González,[a] M. Carmen Ruiz Delgado,[a] Mohammed Al-Hashimi[b] and Rocío Ponce Ortiz*[a]

[a] Department of Physical Chemistry, Faculty of Sciences, University of Málaga, Campus of Teatinos s/n. 29071 Málaga, Spain.

[b] Department of Chemistry, Texas A&M University at Qatar, Education City, Doha, P. O. Box 23874, Qatar.

Table of Contents

Page

1. Methods 2

2. Synthesis and characterization 4

3. DFT calculations 5

4. Variable temperature absorption spectra 12

5. OFETs performance 13

6. Morphologic characterization 15

6.1. GIXRD analysis 15

6.2. AFM images 17

7. Raman spectroscopy 23

8. References 28

1. Methods

OFET fabrication: Field effect transistors were fabricated in a standard bottom gate-top contact architecture with polymers **P1**-**P4** as active layer. First the all, the gate/dielectric substrates (Si/300 nm SiO_2) were double-cleaned by immersing in ethanol with sonication (30 seconds) prior to drying with a stream of N_2 and treating with UV-ozone for 10 min. Then, the surface was functionalized with a self-assembled monolayer of; (i) Hexamethyldisilazane (HMDS), by exposing them to HMDS vapor at room temperature in a closed air-free container under argon conditions for a week. (ii) Octadecyltrichlorosilane (OTS), by immersion of wafers in a 3.0 mM humidity-exposed solution of OTS in hexane for 1 hour prior sonication with hexane, acetone, and finally with ethanol, and dried with an N_2 stream. Then, 5 mg/ml solutions of polymers **P1**, **P2** and **P4** in tetrahidrofuran were deposited both by spin coating and by blade coating, showing enhanced electrical performance the films deposited by spin coating (1500rpm for 60 seconds). On the contrary, thin films of polymer **P3** were prepared by blade coating of a 5 mg/ml solution in chlorobenzene (stirred/heated to 100°C for 15 min) since, in that case, it was not possible to get homogenous films using spin coating. Annealing treatments at different temperatures (100, 150 and 200ºC) were performed on the resulting thin films. Finally, 40 nm gold source and drain electrodes were thermally evaporated through a shadow mask defining different channel widths and lengths. Devices were tested at vacuum conditions by using an EverBeing RF ProbeStation EB-6RF with a 4200-SCS/C Keithley semiconductor characterization system. The tested devices had a channel width of 2000 μm and channel lengths of 60, 80 and 100 μm.

Resonance Raman: Resonance Raman spectra with 532, and 473 nm laser excitations were recorded for thin film samples by using a InVia Qontor Raman Confocal Microscope of Renishaw, which has different diffraction gratings optimized for Visible and Near IR. A CCD detector was used and the Raman scattering radiation was collected in a back-scattering configuration with a 1 cm^{-1} spectral radiation. On the other hand, Resonance Raman spectra with 633 nm laser excitations were recorded by using a Bruker Senterra dispersive Raman microscope equipped with a CCD camera operating at -50ºC, a confocal microscope with a x40 objective, a neon lamp and a Nd:YAG laser. This set up has a spectral resolution of 3–5 cm^{-1}.

FT-Raman: Out-of-Resonance Raman spectra were recorded by using a FT-Raman JASCO (RFT-6000) equipped with an equipped with a InGaAs detector, confocal microscope with a x10 objective and a continuous-wave Nd-YAG laser with excitation at λ=1064 nm.

Grazing Incidence X-Ray Diffraction (GIXRD): GIXDR data using CuKα1 radiation was recorded by using a Bruker D8 DISCOVER diffractometer. The grazing incidence X-ray diffraction setup is equipped with a parabolic Göbel mirror and a conventional line focus Cu radiation tube (40 kV/40 mA). The Cu-kβ line is suppressed by a knife at the exit of the Göbel mirror. The nearly parallel incident beam was collimated with a 2mm primary slit. No primary monochromator is used to improve the monochromaticity of the X-ray beam and to reduce the beam divergence after the Göbel mirror. Soller slits were used

to reduce the axial divergence (divergence in the plane perpendicular to the diffraction plane) of the X-ray beam. This axial divergence is then reduced to 2.5°. The sample is mounted on a motorized goniometric head. Omega and chi scans are performed to align the sample along the incident beam. The z scan ensures that the sample is aligned along the incident beam with an error lower than 10 µm. The accuracy of the alignment of the sample obtained after performing different rocking curves is lower than 5/100°. The diffracted beam is collected by a Scintillation detector. No radial Soller slits nor analyser crystal is mounted in front of the detector. Measurements were made from 2 to 35º (2θ) during 120 minutes. The tube worked at 40 kV and 40 mA. The omega value was determined by several omega scanning at the two-theta main peak of the polimer´s thin film.

Atomic Force Microscopy (AFM): thin films were recorded by a Multimode atomic force microscope with a Nanoscope V Controller (Bruker Corporation, Billerica, MA, USA) working in tapping mode.

Computational methodology: The optimum structures of the monomeric and dimeric models of **P1**-**P4** polymers under study were performed at the framework of the Density Functional Theory (DFT) using the hybrid, generalized gradient approximation (GGA) functional B3LYP[1] and the long-range corrected hybrid ωB97XD[2] functional together with the 6-31G**[3] basis set, as implemented in the GAUSSIAN16 program.[4] To further understand the conformation of the systems under study, a relaxed potential energy hypersurface was computed around the interactions of interest for monomeric units of **P1**-**P4** by constraining the angle of the selected dihedral bonds (by step of 10^{o}) and allowing all other degrees of freedom to relax to their potentially energy minima. The resulting potential energy curves were then referenced to the minimal energy structure. Since a better agreement with the theoretical Raman spectra was obtained for “anti” conformation of the IIG-thiophene linkage, we have then selected these conformations for the construction of the dimers.

For the calculations of the dimers, all geometrical parameters were allowed to vary independently. Harmonic frequencies calculations were performed on the resulting optimized geometries and no imaginary frequencies were observed, which ensures the finding of the global minimum energy. Note that, Raman intensities were calculated by using an adjustment of the theoretical force fields in which the frequencies are uniformly scaled down by a factor of 0.972 to disentangle experimental misassignments. The theoretical spectra were obtaining by convolution the scaled frequencies and the Raman scattering activities with Gaussian functions (10 cm^{-1} width at the half-height). Molecular orbitals distribution and vibrational eigenvectors were plotted using the ChemCraft 1.8 molecular modelling software.[5] On the previously optimized molecular geometries, vertical electronic excitation energies were computed by using the time-dependent DFT (TD-DFT) approach.[6] Interestingly, both B3LYP and ωB97X-D functionals predict comparable results for the optical and electronic properties.

Gel Permeation Chromatography (GPC): Number-average (M_n) and weight average (M_w) were determined by Agilent Technologies 1200 series GPC running in

chlorobenzene at 80 °C, using two PL mixed B columns in series, and calibrated against narrow polydispersity polystyrene standards.

UV-vis spectroscopy (UV-vis): UV-vis spectra were recorded from 1000 nm to 350 nm on a UV- 1601 Shimadzu UV-vis spectrometer for samples in 10^{-4} M chlorobenzene solution and thin film.

Cyclic voltammetry (CV) measurements of polymers films were performed under argon atmosphere using a CHI760E Voltammetry analyzer with 0.1 M tetra-n-butylammonium hexafluorophosphate in acetonitrile as the supporting electrolyte. A platinum disk working electrode, a platinum wire counter electrode, and a silver wire reference electrode were employed, and the ferrocene/ferrocenium (Fc/Fc+) was used as the internal reference for all measurements. The scanning rate was 100 mV/s. Polymer films were drop-casted from chlorobenzene solutions on a Pt working electrode (2 mm in diameter).

2. Synthesis

As depicted in **Scheme S1** copolymers **P1-P4** were synthesized using Stille cross-coupling polymerization of isoindigo monomers (**M1** and **M2)** with the respective BT monomers (**M3** and **M4**) in a microwave reactor in chlorobenzene using $Pd(PPh_3)_4$ as the catalyst. All copolymers were precipitated in acidified methanol and purified via Soxhlet extraction with a sequence of refluxing methanol, acetone and chloroform. Copolymers **P1-P4** were collected in chlorobenzene solution and isolated as blue dark solids.

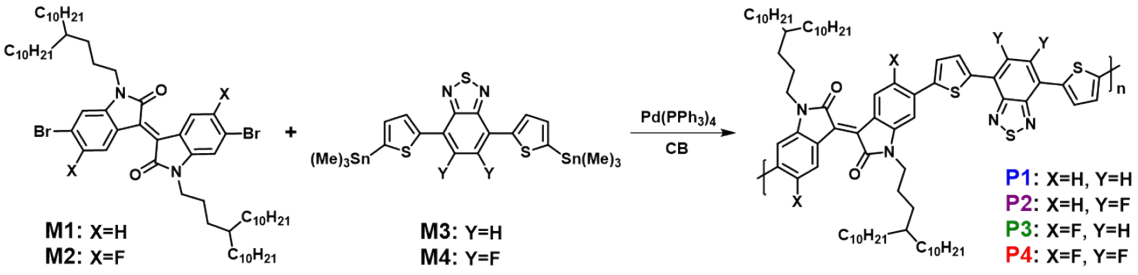

Scheme S1. Synthesis of **P1-P4**.

All commercially available solvents, reagents, and chemicals were used as received without further purification unless otherwise stated. All operations and reactions were carried out under argon using standard Schlenk line techniques. Microwave experiments were performed in a Biotage initiator V 2.3.

3. DFT Calculations

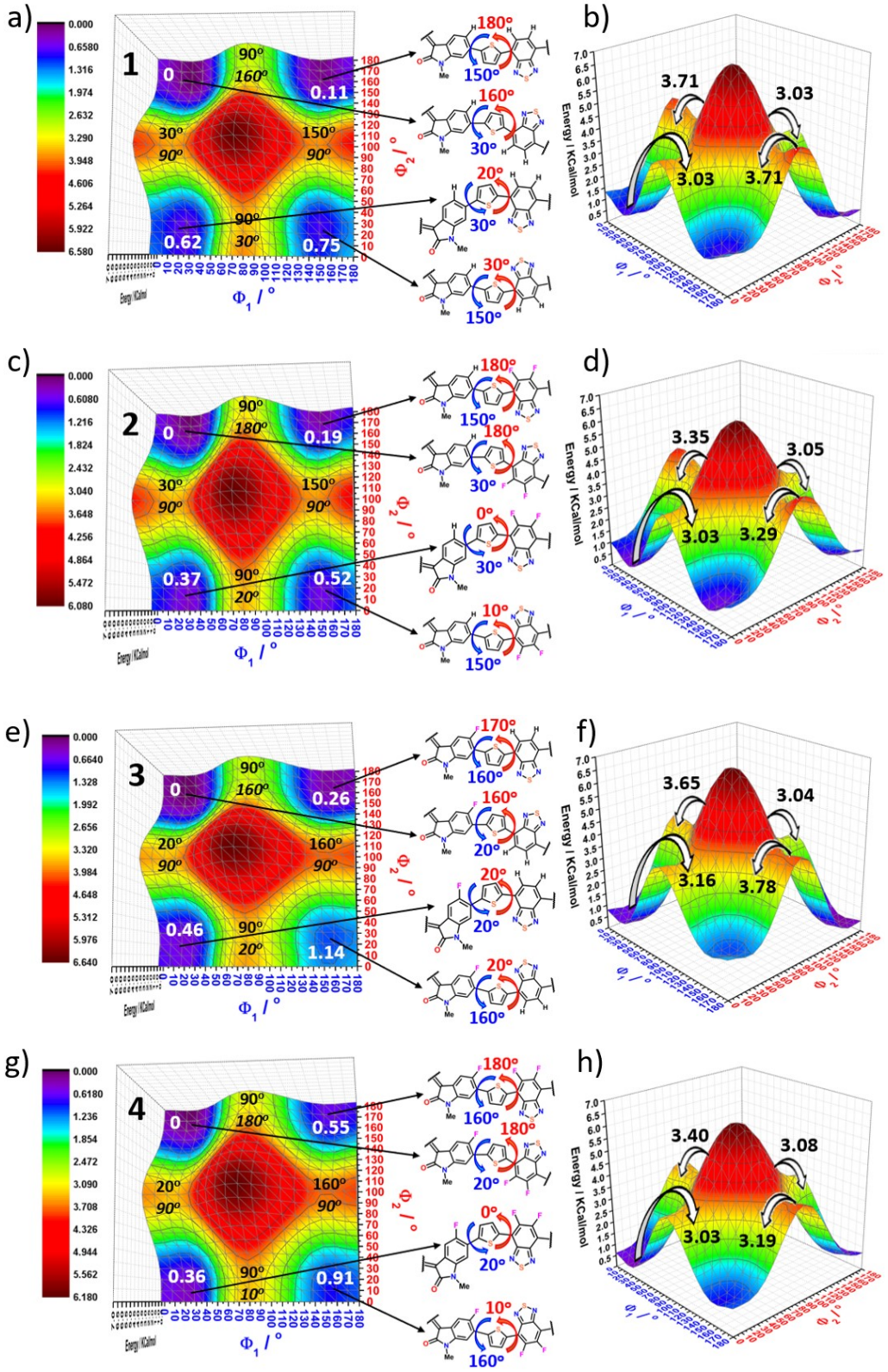

Figure S1. Dihedral potential energy hypersurface E=E(ϕ_1,ϕ_2) calculated for a monomeric model of **P1** (a-b), **P2** (c-d), **P3** (e-f) and **P4** (g-h) at the ωB97XD/6-31G** level. Dihedral angle values of the four possible conformers at the minima energy and their energy differences with respect

the most stable conformer (white numbers) of **P1** (a), **P2** (c), **P3** (e) and **P4** (g). The energetic barrier between the four conformers of **P1** (b), **P2** (d), **P3** (f) and **P4** (h) are also shown.

For polymeric systems, backbone conformation strongly depends on the rotational freedom of the single bonds connecting the (hetero)arene moieties. Thus, a preliminary study of the dihedral potential energy hypersurfaces relative to the rotations of the isoindigo-based acceptor moiety with respect the adjacent donor thiophene ring (ϕ_1, IIG-T) and between the thiophene and the BTD acceptor moiety (ϕ_2, BTD-T) were computed at DFT level for monomeric models of **P1**-**P4** to further understand the conformation of these systems. The results reveal an absolute minimum of potential energy, in which sulfur atom of the thiophene ring is oriented toward the proximal hydrogen (**P1** and **P3**) or fluorine (**P2** and **P4**) atoms of the BTD acceptor moiety, which indicated that the S•••H and S•••F interactions may be stronger than that of S•••N interactions. On the other hand, the IIG-T linkage does not show a clear preferent conformation, with the "syn" and "anti" conformations quite near in energy and invariant energetic barriers between them upon fluorination. Interestingly, the minima of the potential energy hypersurfaces are becoming narrower by the progressive fluorination, meaning that S•••F interactions are playing a key role on the backbone coplanarity. The minimum energy conformers were next used to model the dimeric structures corresponding to the respective **P1**-**P4** backbones.

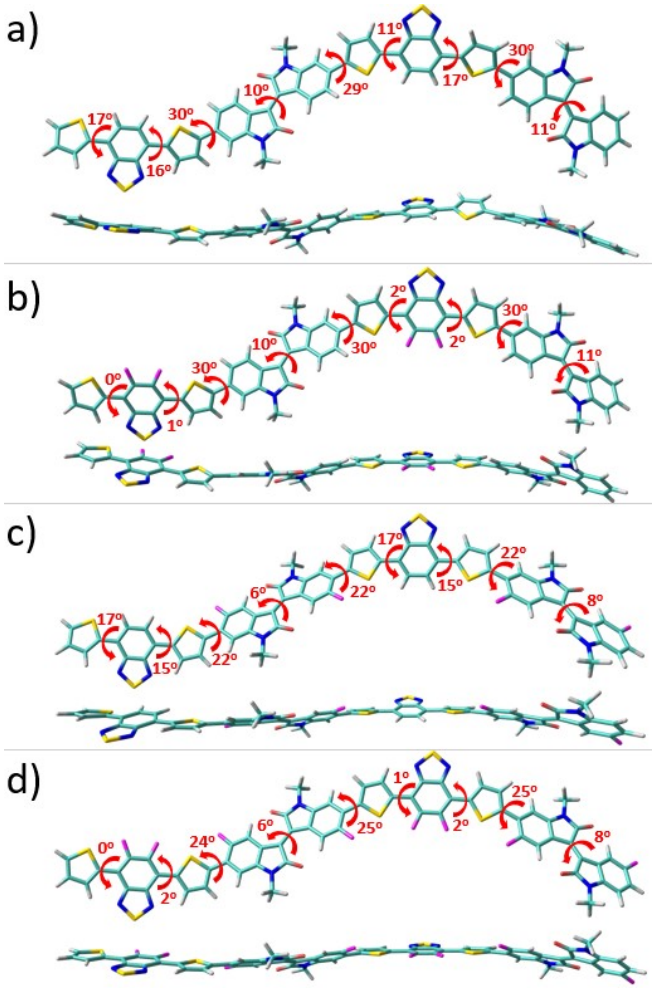

Figure S2. Top and lateral views of the optimized geometries (ωB97XD/6-31G** level of theory) for dimeric models of **P1** (a), **P2** (b), **P3** (c) and **P4** (d) polymers. The dihedral angles values between selected rings are also shown.

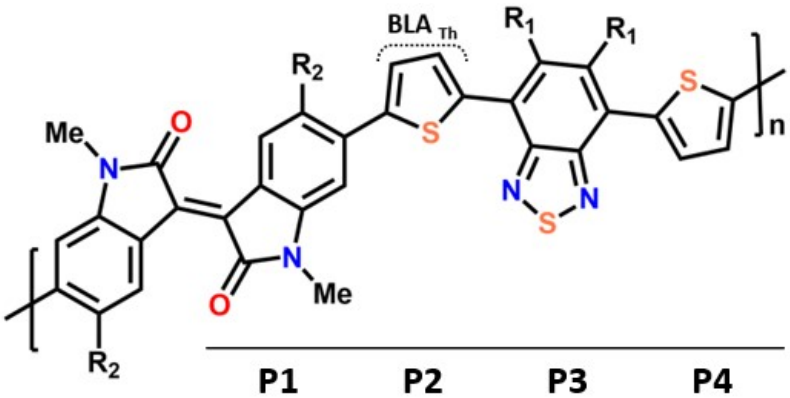

	P1	P2	P3	P4
R_1	H	F	H	F
R_2	H	H	F	F
BLA_{Th}	0.030	0.025	0.022	0.018

Figure S3. DFT-calculated Bond Length Alternation (BLA) values given in angstroms for selected parts of systems under study. The calculations were performed at the B3LYP/6-31G** level.

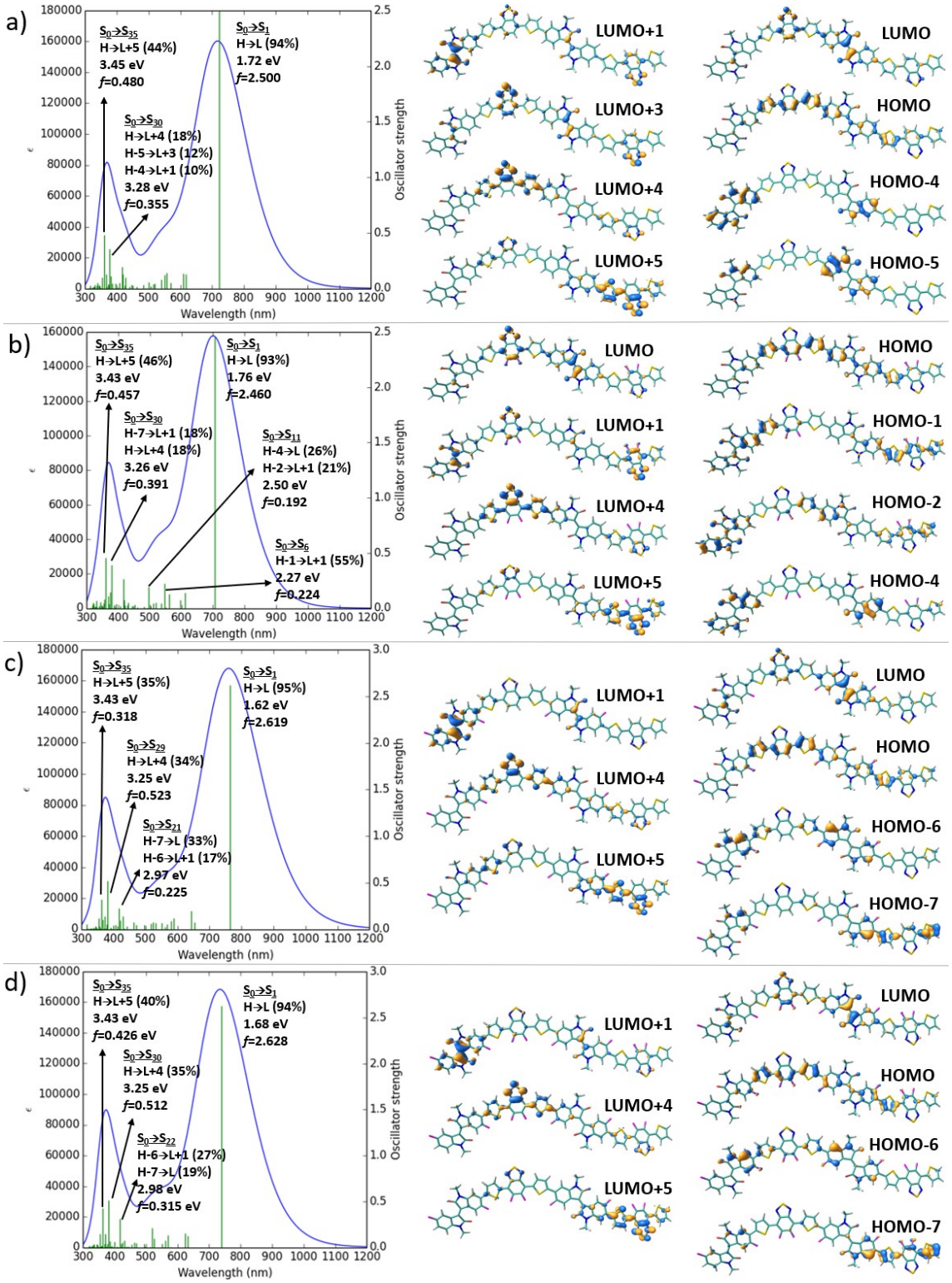

Figure S4. DFT-calculated vertical excited state transitions (green solid bars) at the B3LYP/6-31G** level for dimeric models of **P1** (a), **P2** (b), **P3** (c) and **P4** (d) polymers. The frontier molecular orbitals topologies involved in the main electronic transitions are also shown.

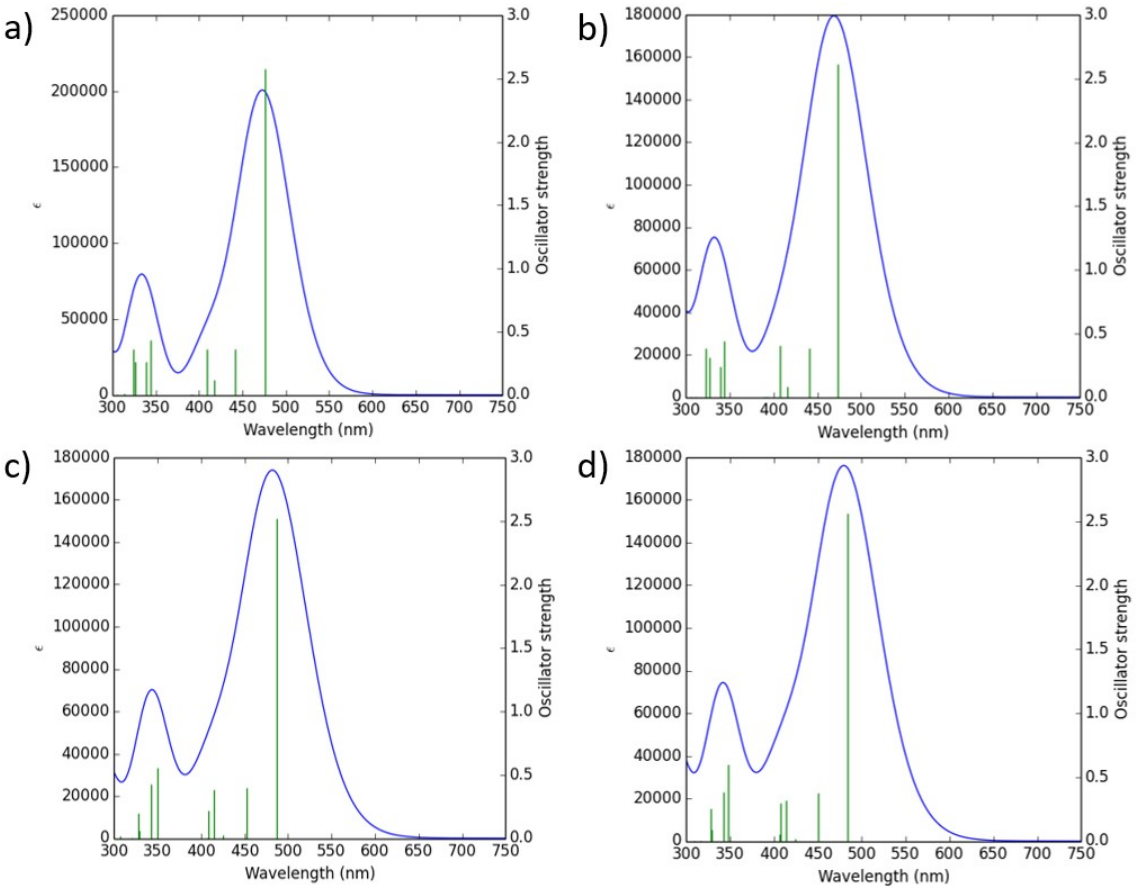

Figure S5. Simulated absorption spectra and main excitations (shown as vertical bars) for dimeric models of **P1** (a), **P2** (b), **P3** (c) and **P4** (d) polymers. The computations were done at the TD-DFT level, by using ωB97XD functional and 6-31G** basis set.

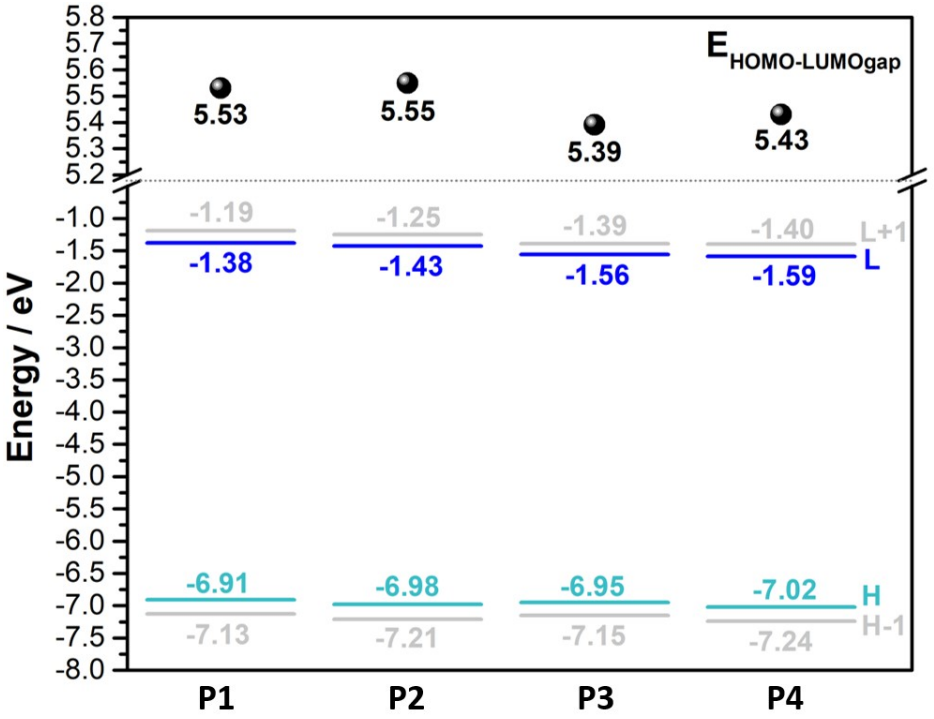

Figure S6. DFT-calculated molecular orbital energies for dimeric models of **P1**, **P2**, **P3** and **P4** polymers at the ωB97XD/6-31G** level of theory.

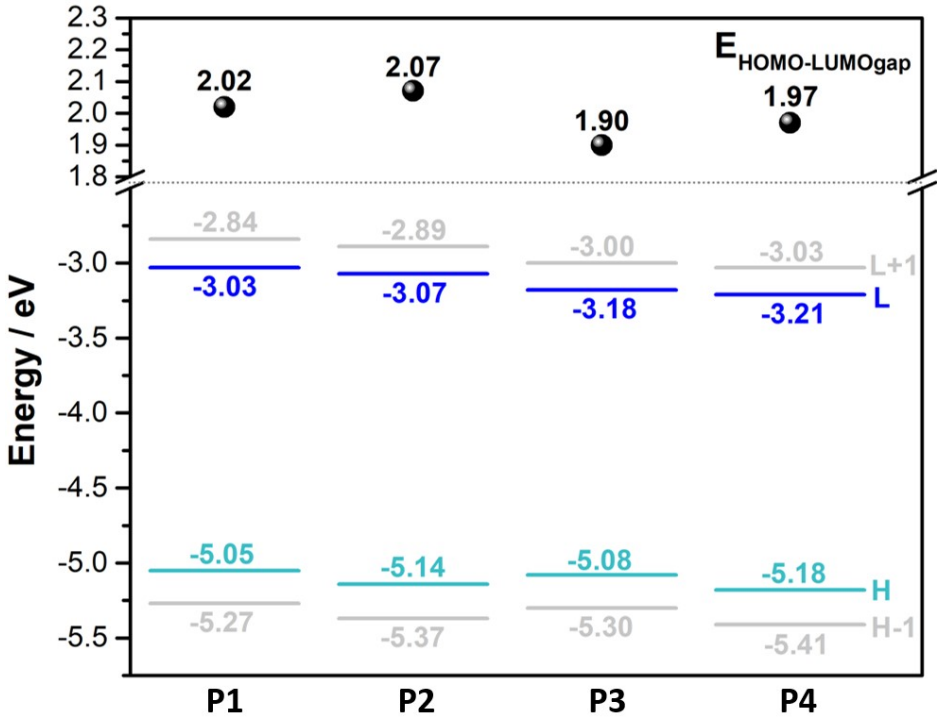

Figure S7. DFT-calculated molecular orbital energies for dimeric models of **P1**, **P2**, **P3** and **P4** polymers at the B3LYP/6-31G** level of theory.

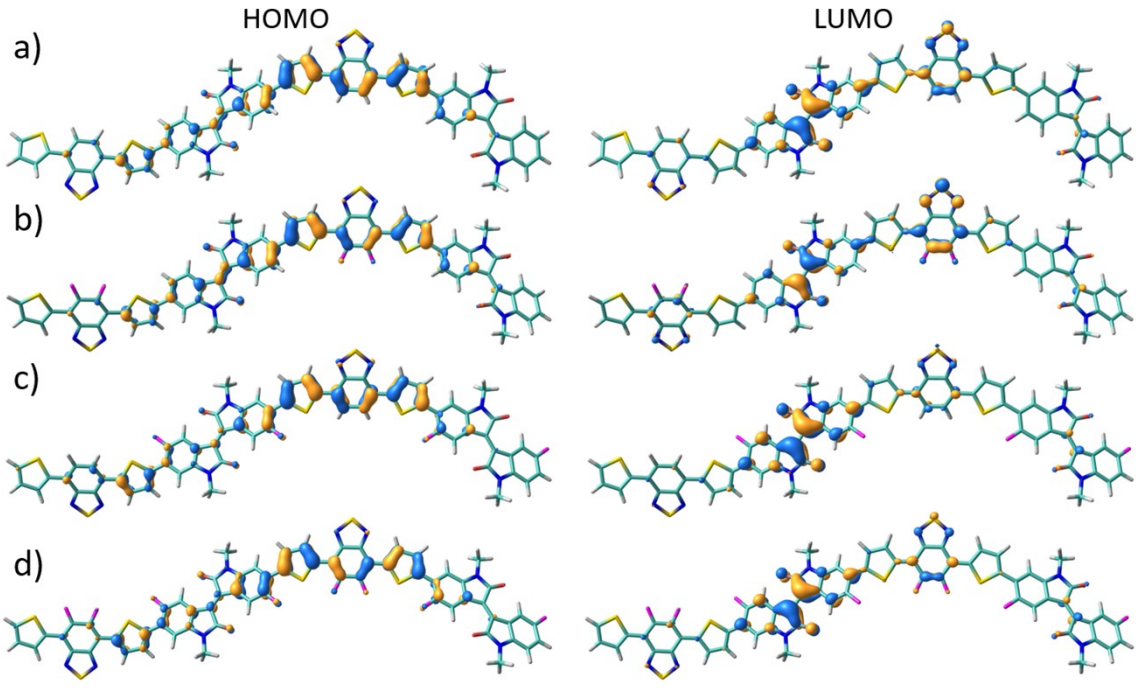

Figure S8. DFT-calculated HOMO (right) and LUMO (left) topologies for dimeric models of **P1** (a), **P2** (b), **P3** (c) and **P4** (d) polymers at the ωB97XD/6-31G** level of theory.

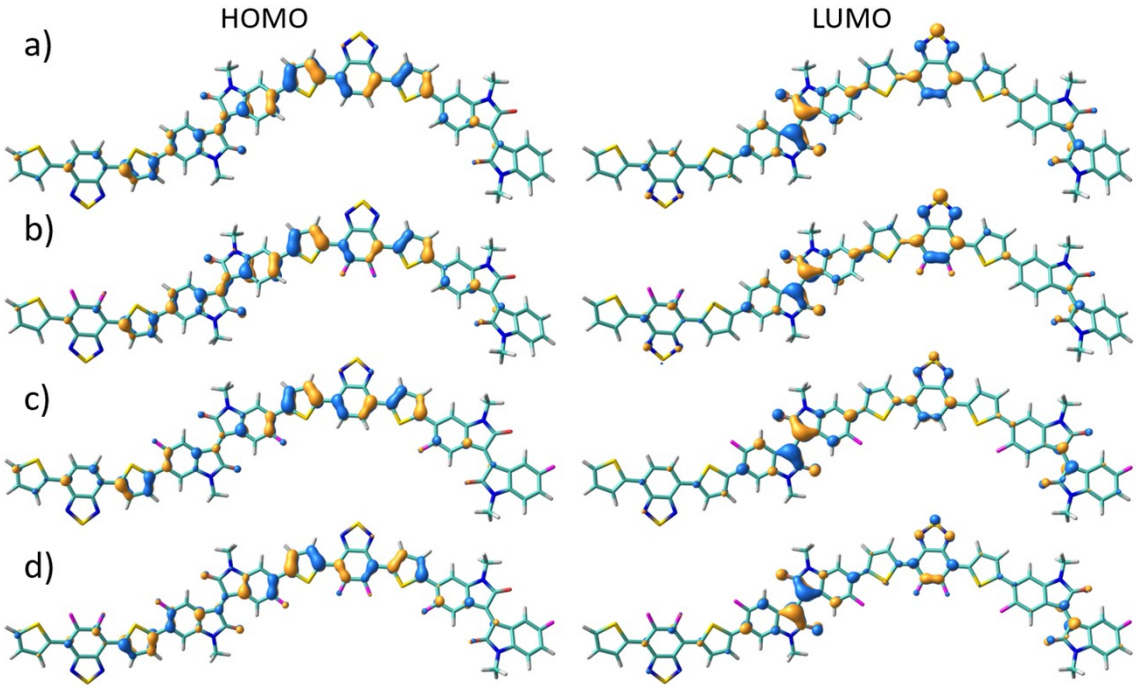

Figure S9. DFT-calculated HOMO (right) and LUMO (left) topologies for dimeric models of **P1** (a), **P2** (b), **P3** (c) and **P4** (d) polymers at the B3LYP/6-31G** level of theory.

4. Variable temperature absorption spectra

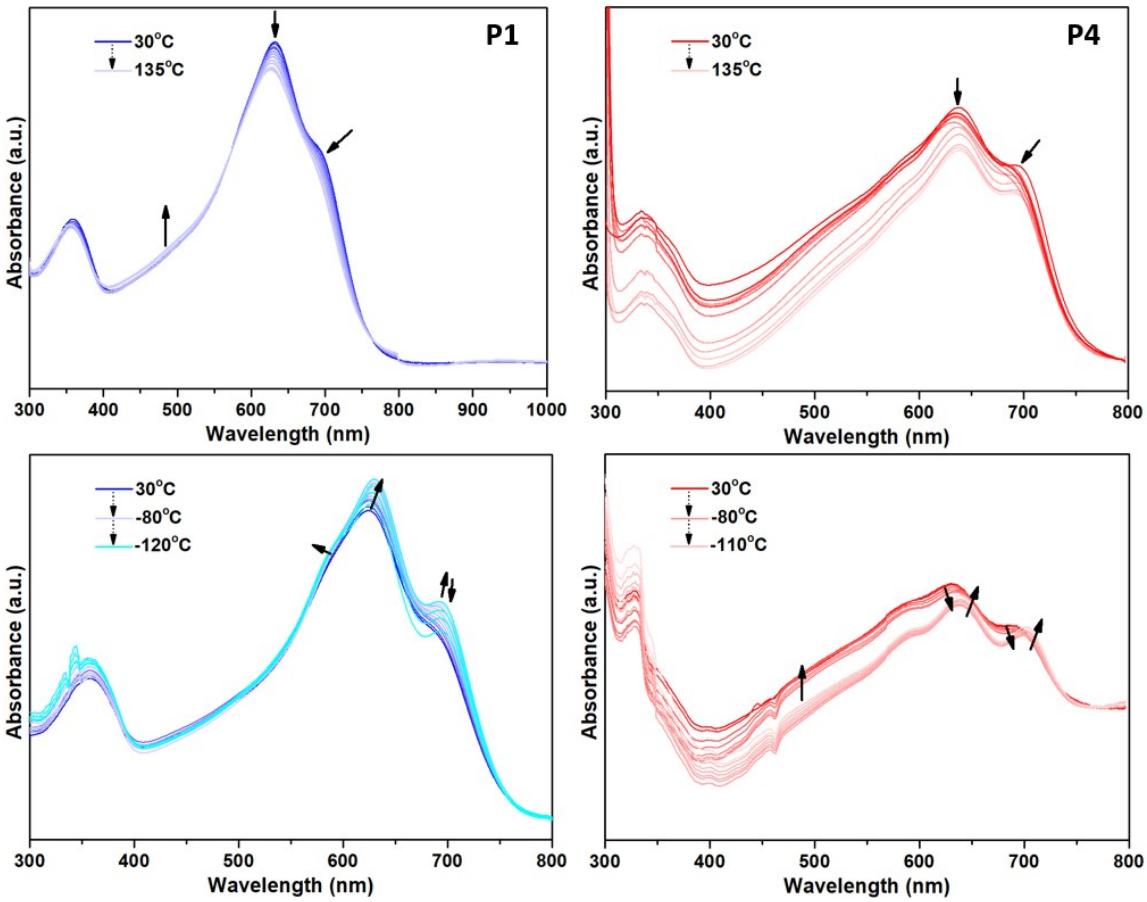

Figure S10. Variable temperature absorption spectra of **P1** (blue) and **P4** (red) polymers in diluted chlorobenzene (for heating) and 2-methyl tetrahydrofuran (for cooling) solutions.

5. OFETs performance

Table S1. P-channel OFET derived electrical data for polymer **P1** deposited films under different conditions. Average and the best values (in parenthesis) are shown. The average values were obtained from at least 6 devices for each material.

Subst. treatment	Thermal Annealing	μ_h ($cm^2 V^{-1} s^{-1}$)	I_{ON}/I_{OFF}	V_T(V)
OTS	RT	1.35×10^{-5} (2.20×10^{-5})	3×10^{1} (4×10^{1})	8 (5)
	100°, 2h	6.30×10^{-6} (1.53×10^{-5})	4 (6)	31 (24)
	150°, 2h	1.09×10^{-5} (1.43×10^{-5})	8×10^{1} (1×10^{2})	4 (-3)
	200°, 2h	3.57×10^{-5} (4.03×10^{-5})	5×10^{1} (6×10^{1})	1 (0)
HMDS	RT	5.70×10^{-6} (9.52×10^{-6})	2×10^{1} (6×10^{1})	22 (0)
	100°, 2h	8.64×10^{-6} (1.11×10^{-5})	1×10^{1} (2×10^{1})	24 (7)
	150°, 2h	1.01×10^{-5} (1.30×10^{-5})	5×10^{1} (1×10^{2})	3 (1)
	200°, 2h	1.51×10^{-5} (2.54×10^{-5})	4×10^{1} (4×10^{1})	43 (31)
No. treatment	RT	--	--	--
	100°, 2h	--	--	--
	150°, 2h	--	--	--
	200°, 2h	--	--	--

Table S2. OFET derived electrical data for polymer **P2** deposited films under different conditions. Average and the best values (in parenthesis) are shown. The average values were obtained from at least 6 devices for each material.

		N-channel			P-channel		
Subst. treatment	Thermal Annealing	μ_e ($cm^2 V^{-1} s^{-1}$)	I_{ON}/I_{OFF}	V_T(V)	μ_h ($cm^2 V^{-1} s^{-1}$)	I_{ON}/I_{OFF}	V_T(V)
OTS	RT	4.13×10^{-4} (6.29×10^{-4})	1×10^{3} (2×10^{3})	49 (43)	3.02×10^{-4} (4.24×10^{-4})	2×10^{3} (3×10^{3})	-10 (-17)
	150°, 2h	3.80×10^{-3} (4.03×10^{-3})	4×10^{3} (9×10^{3})	58 (52)	2.89×10^{-3} (3.32×10^{-3})	1×10^{3} (2×10^{3})	-1 (-17)
	200°, 2h	1.13×10^{-3} (1.45×10^{-3})	3×10^{2} (4×10^{2})	56 (49)	1.20×10^{-3} (1.65×10^{-3})	1×10^{3} (1×10^{3})	-35 (-42)
HMDS	RT	--	--	--	6.54×10^{-6} (7.40×10^{-6})	1×10^{3} (6×10^{3})	-12 (-21)
	100°, 2h	--	--	--	2.33×10^{-6} (3.56×10^{-6})	1×10^{1} (5×10^{1})	9 (4)
	150°, 2h	--	--	--	1.18×10^{-5} (1.93×10^{-5})	2×10^{3} (6×10^{3})	-13 (-18)
	200°, 2h	--	--	--	2.94×10^{-5} (3.25×10^{-5})	7×10^{1} (1×10^{2})	-19 (-20)
No. treatment	RT	--	--	--	--	--	--
	100°, 2h	--	--	--	--	--	--
	150°, 2h	--	--	--	--	--	--
	200°, 2h	--	--	--	--	--	--

Table S3. OFET derived electrical data for polymer **P3** deposited films under different conditions. Average and the best values (in parenthesis) are shown. The average values were obtained from at least 6 devices for each material.

		N-channel			P-channel		
Subst. treatment	**Thermal Annealing**	μ_e ($cm^2 V^{-1} s^{-1}$)	I_{ON}/I_{OFF}	V_T(V)	μ_h ($cm^2 V^{-1} s^{-1}$)	I_{ON}/I_{OFF}	V_T(V)
OTS	**RT**	5.29×10^{-2} (7.90×10^{-2})	9×10^{1} (1×10^{2})	48 (36)	7.03×10^{-2} (9.73×10^{-2})	1×10^{2} (3×10^{2})	-13 (-18)
	100°, 2h	7.48×10^{-2} (7.98×10^{-2})	9×10^{1} (2×10^{2})	49 (45)	7.41×10^{-2} (8.18×10^{-2})	1×10^{2} (2×10^{2})	-14 (-19)
	200°, 2h	9.76×10^{-2} (1.06×10^{-1})	8×10^{1} (1×10^{2})	57 (53)	1.20×10^{-1} (1.45×10^{-1})	2×10^{2} (4×10^{2})	-26 (-31)
HMDS	**RT**	7.13×10^{-2} (7.80×10^{-2})	3×10^{1} (3×10^{1})	37 (33)	8.84×10^{-2} (1.01×10^{-1})	3×10^{1} (4×10^{1})	-20 (-24)
	100°, 2h	5.85×10^{-2} (7.46×10^{-2})	2×10^{1} (2×10^{1})	31 (27)	6.41×10^{-2} (8.39×10^{-2})	2×10^{1} (3×10^{1})	-16 (-19)
	150°, 2h	9.41×10^{-2} (1.01×10^{-1})	3×10^{1} (5×10^{1})	35 (27)	1.24×10^{-1} (1.36×10^{-2})	4×10^{1} (5×10^{1})	-23 (-28)
	200°, 2h	9.39×10^{-2} (1.01×10^{-1})	1×10^{1} (1×10^{1})	28 (26)	1.06×10^{-1} (1.14×10^{-1})	1×10^{1} (1×10^{1})	-12 (-13)
No. treatment	**RT**	--	--	--	--	--	--
	100°, 2h	--	--	--	--	--	--
	150°, 2h	--	--	--	--	--	--
	200°, 2h				--	--	--

Table S4. OFET derived electrical data for polymer **P4** deposited films under different conditions. Average and the best values (in parenthesis) are shown. The average values were obtained from at least 6 devices for each material.

		N-channel			P-channel		
Subst. treatment	**Thermal Annealing**	μ_e ($cm^2 V^{-1} s^{-1}$)	I_{ON}/I_{OFF}	V_T(V)	μ_h ($cm^2 V^{-1} s^{-1}$)	I_{ON}/I_{OFF}	V_T(V)
OTS	**RT**	1.12×10^{-2} (1.30×10^{-2})	2×10^{3} (7×10^{3})	17 (8)	1.27×10^{-2} (1.57×10^{-2})	7×10^{5} (3×10^{6})	-21 (-29)
	150°, 2h	2.09×10^{-2} (2.44×10^{-2})	9×10^{1} (2×10^{2})	13 (7)	3.32×10^{-2} (7.35×10^{-2})	1×10^{5} (4×10^{5})	-11 (-29)
	200°, 2h	1.39×10^{-2} (1.90×10^{-2})	1×10^{3} (2×10^{3})	37 (32)	6.14×10^{-2} (1.05×10^{-1})	3×10^{4} (4×10^{4})	-17 (-29)
HMDS	**RT**	8.01×10^{-3} (1.05×10^{-2})	2×10^{2} (3×10^{2})	27 (23)	9.30×10^{-3} (1.16×10^{-2})	4×10^{4} (1×10^{5})	-16 (-25)
	100°, 2h	5.96×10^{-3} (7.01×10^{-3})	5×10^{1} (7×10^{1})	33 (21)	8.41×10^{-3} (8.77×10^{-3})	9×10^{3} (1×10^{4})	-26 (-28)
	150°, 2h	1.24×10^{-2} (1.39×10^{-2})	1×10^{2} (1×10^{2})	27 (24)	1.28×10^{-2} (1.37×10^{-2})	5×10^{6} (1×10^{7})	-16 (-21)
	200°, 2h	2.70×10^{-2} (3.40×10^{-2})	5×10^{1} (9×10^{1})	33 (31)	3.27×10^{-2} (4.27×10^{-2})	7×10^{4} (1×10^{5})	-24 (-33)
No. treatment	**RT**	3.37×10^{-5} (4.16×10^{-5})	7×10^{1} (1×10^{2})	7 (1)	6.41×10^{-4} (7.46×10^{-4})	6×10^{2} (1×10^{3})	-22 (-27)
	100°, 2h	1.06×10^{-4} (1.68×10^{-4})	4×10^{2} (1×10^{3})	26 (18)	9.37×10^{-4} (2.02×10^{-3})	1×10^{3} (1×10^{3})	-21 (-38)
	150°, 2h	8.06×10^{-5} (1.00×10^{-4})	2×10^{2} (2×10^{2})	32 (18)	7.28×10^{-4} (1.04×10^{-3})	9×10^{2} (2×10^{3})	-27 (-30)
	200°, 2h	7.71×10^{-4} (1.36×10^{-3})	1×10^{2} (2×10^{2})	49 (22)	2.42×10^{-3} (3.29×10^{-3})	1×10^{3} (1×10^{3})	-38 (-44)

6. Morphologic characterization

6.1 GIXRD analysis

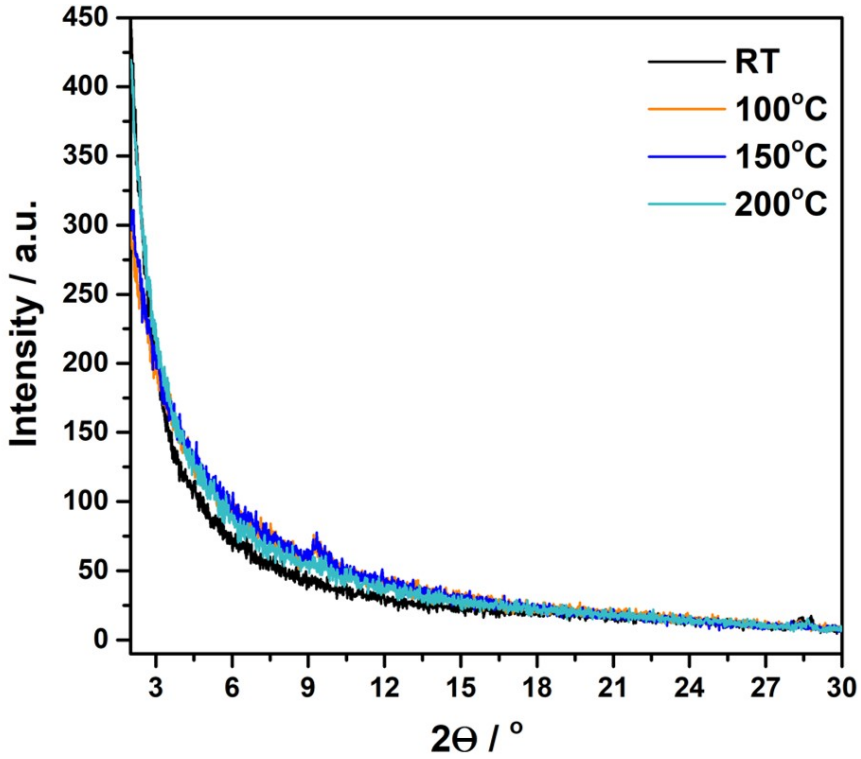

Figure S11. GIXRD patterns of thin films of **P1** on OTS treated Si/SiO2 substrates and annealed at different temperatures.

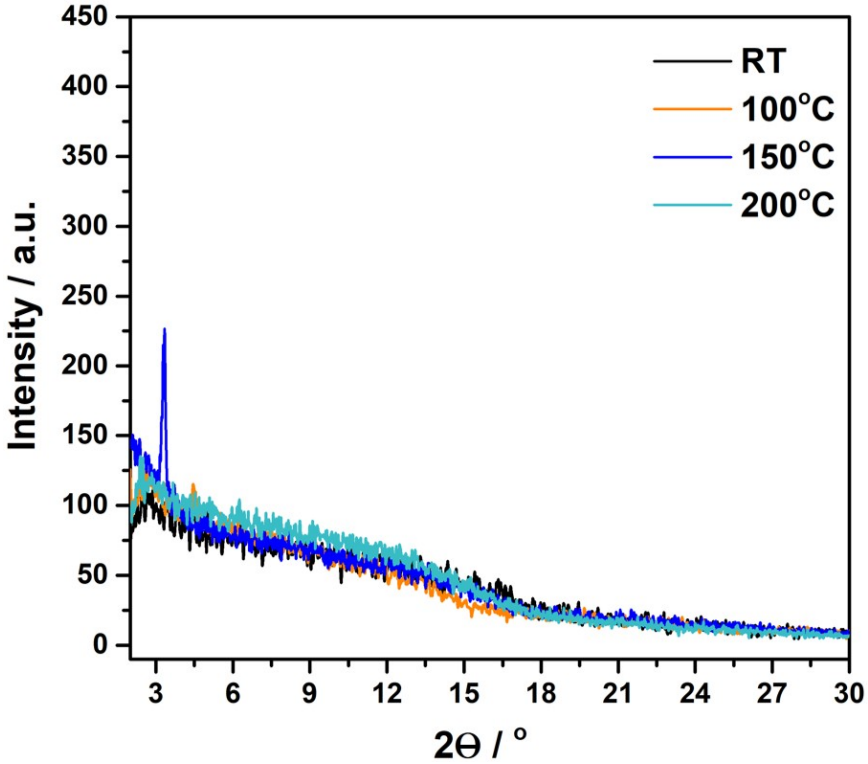

Figure S12. GIXRD patterns of thin films of **P2** on OTS treated Si/SiO2 substrates and annealed at different temperatures.

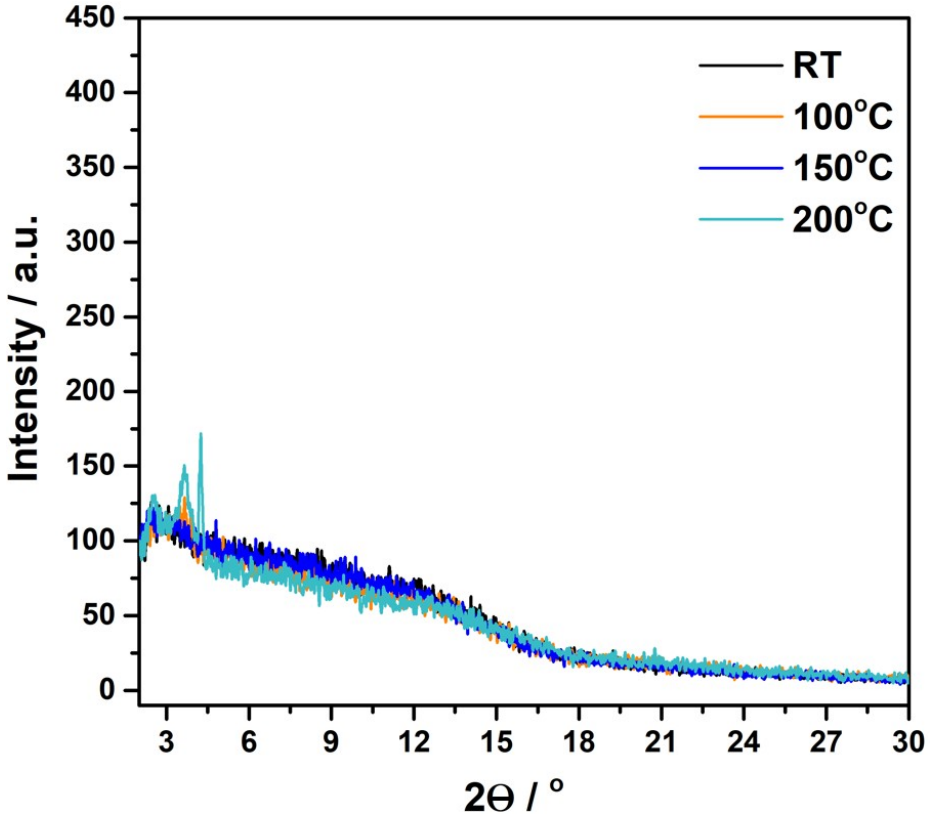

Figure S13. GIXRD patterns of thin films of **P3** on OTS treated Si/SiO2 substrates and annealed at different temperatures.

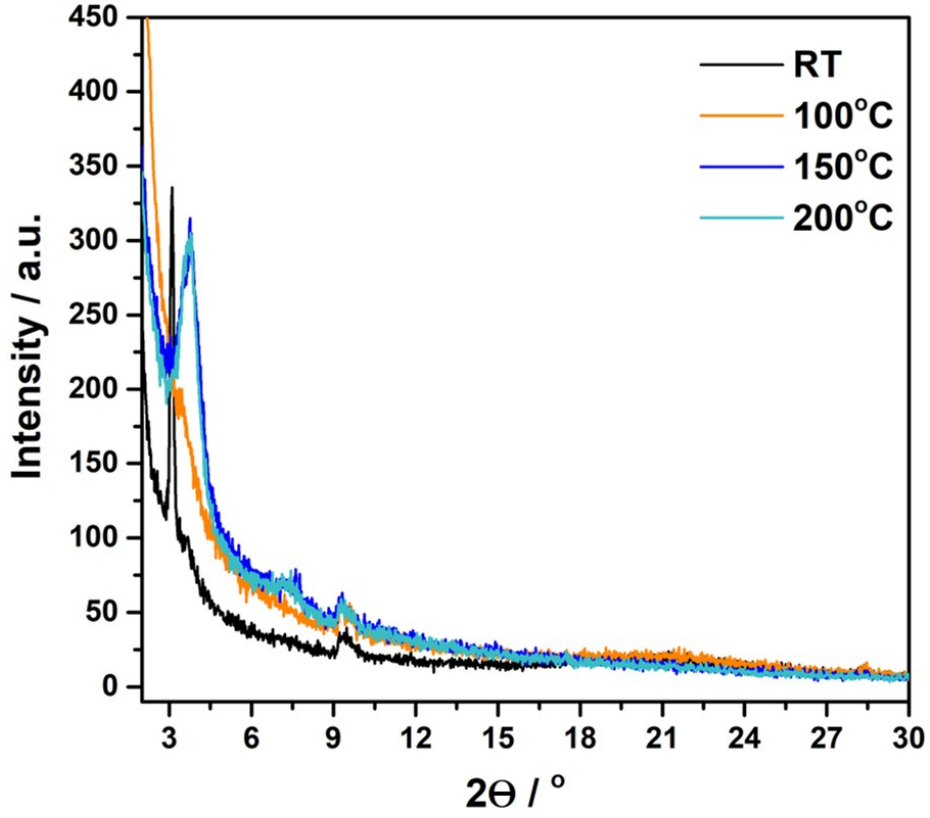

Figure S14. GIXRD patterns of thin films of **P4** on OTS treated Si/SiO2 substrates and annealed at different temperatures.

6.2 AFM images

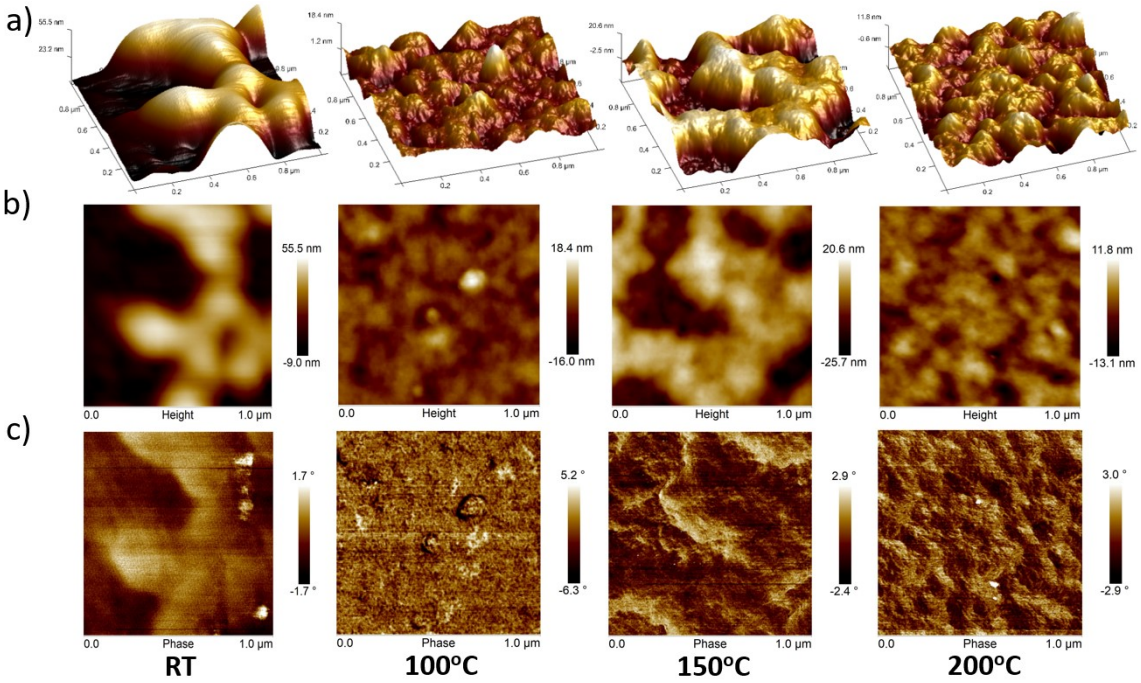

Figure S15. Tapping-mode AFM images of (a) 3D-topography, (b) height and (c) phase in 1 µm x 1 µm scan size of thin films of **P1** deposited on OTS-treated Si/SiO_2 substrates annealed at different temperatures.

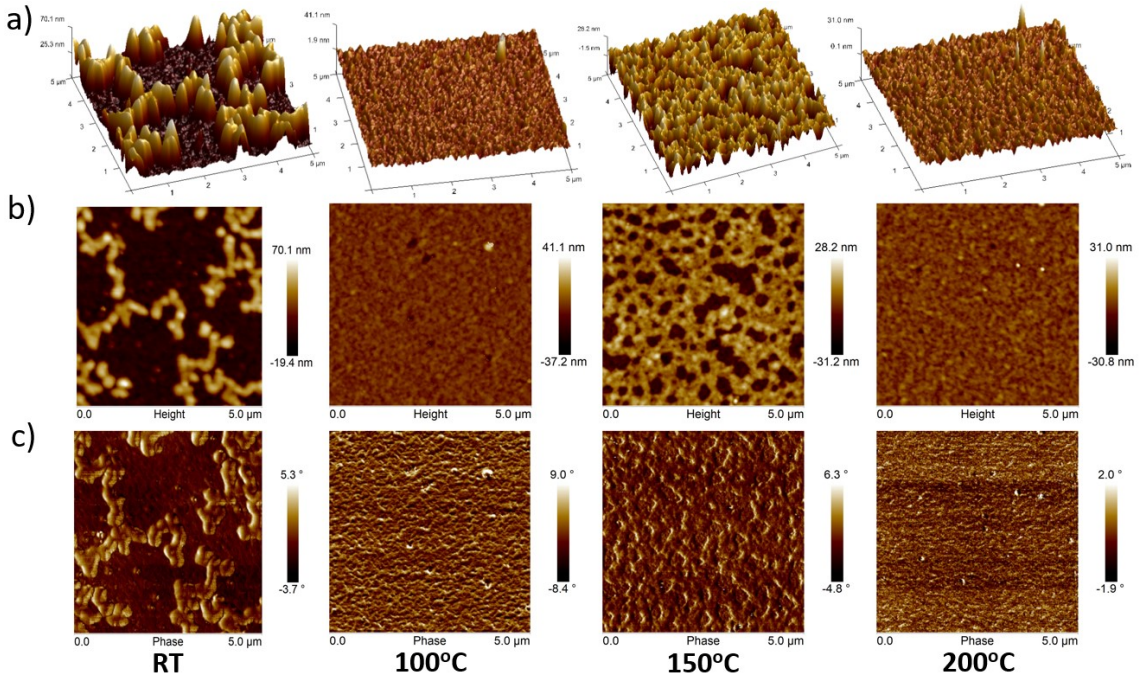

Figure S16. Tapping-mode AFM images of (a) 3D-topography, (b) height and (c) phase in 5 µm x 5 µm scan size of thin films of **P1** deposited on OTS-treated Si/SiO_2 substrates annealed at different temperatures.

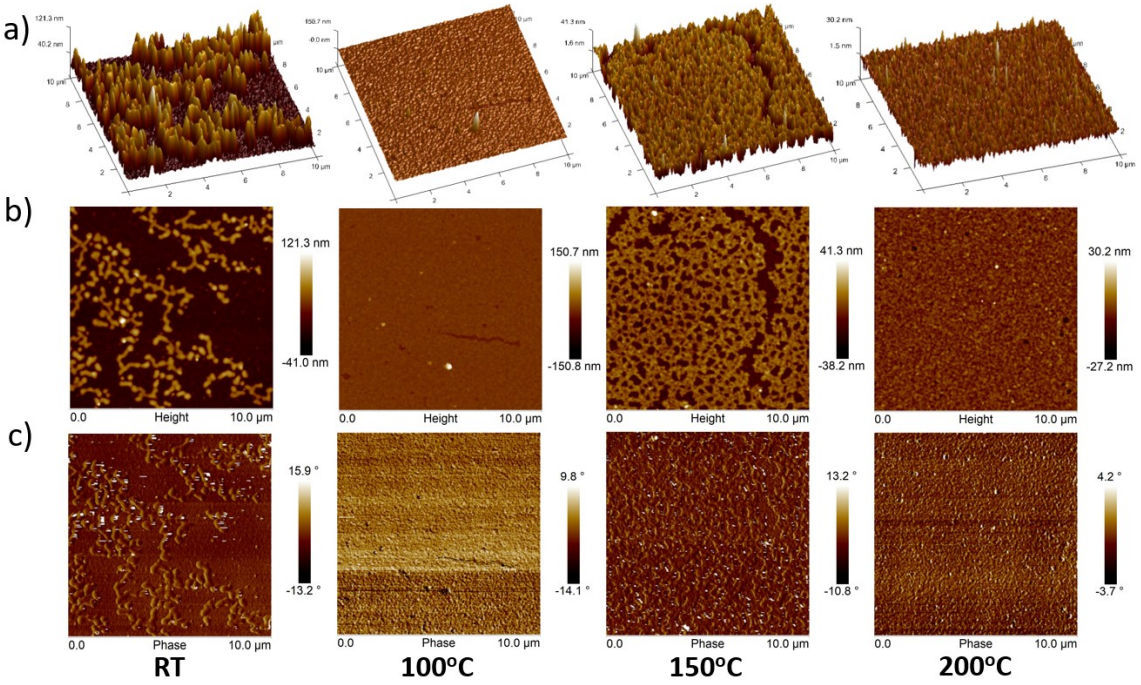

Figure S17. Tapping-mode AFM images of (a) 3D-topography, (b) height and (c) phase in 10 µm x 10 µm scan size of thin films of **P1** deposited on OTS-treated Si/SiO_2 substrates annealed at different temperatures.

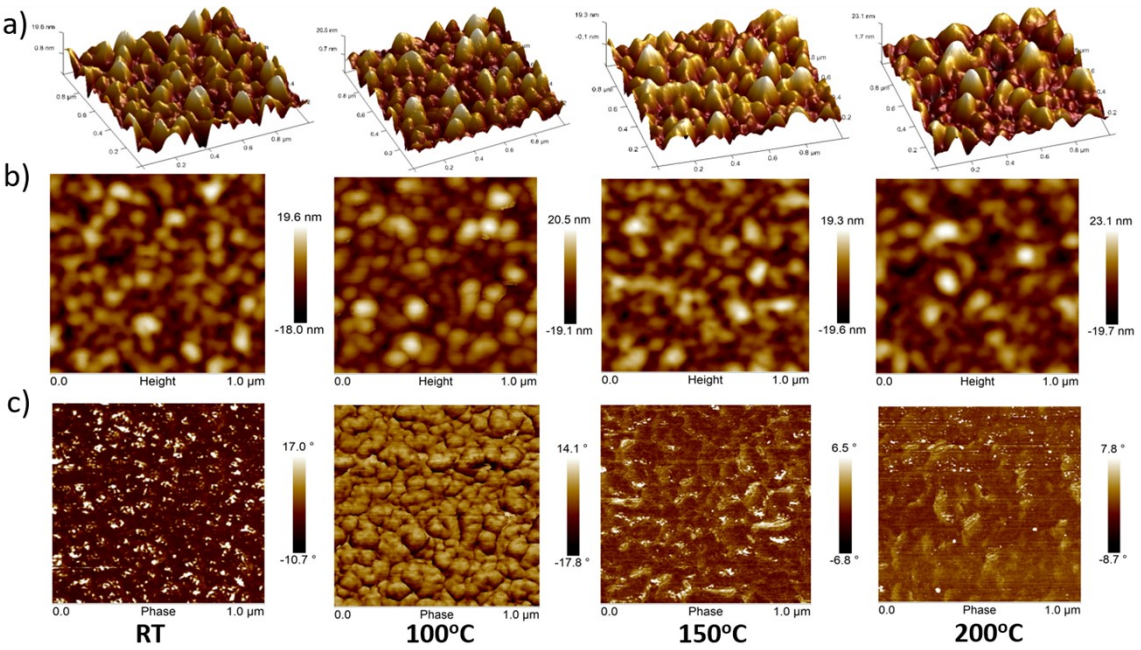

Figure S18. Tapping-mode AFM images of (a) 3D-topography, (b) height and (c) phase in 1 µm x 1 µm scan size of thin films of **P2** deposited on OTS-treated Si/SiO_2 substrates annealed at different temperatures.

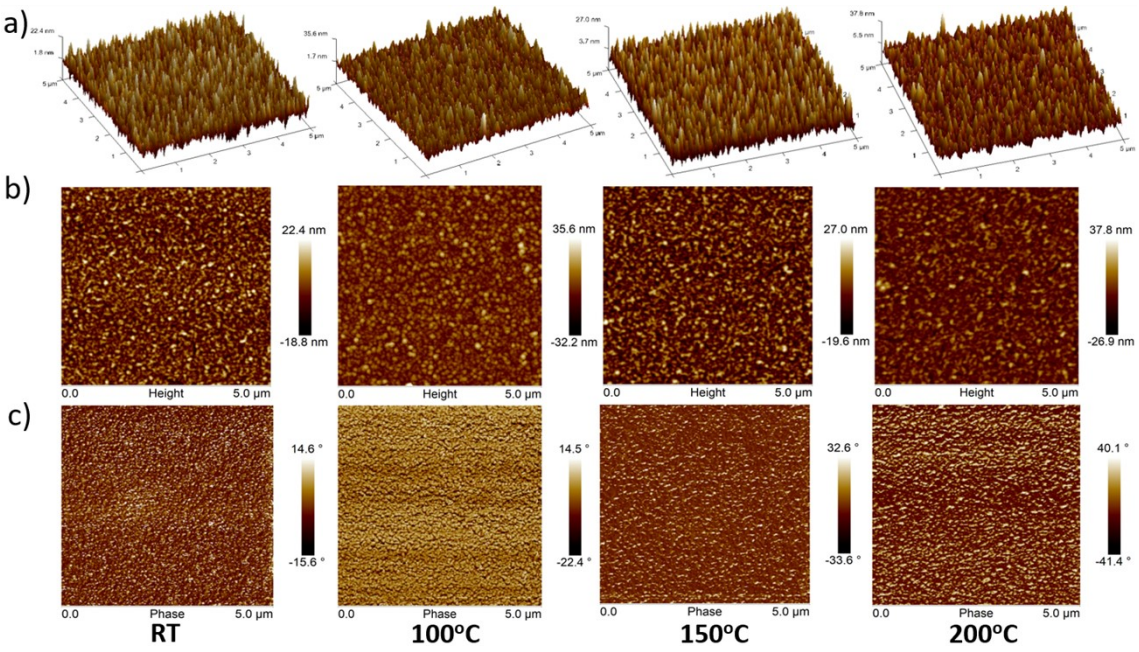

Figure S19. Tapping-mode AFM images of (a) 3D-topography, (b) height and (c) phase in 5 µm x 5 µm scan size of thin films of **P2** deposited on OTS-treated Si/SiO_2 substrates annealed at different temperatures.

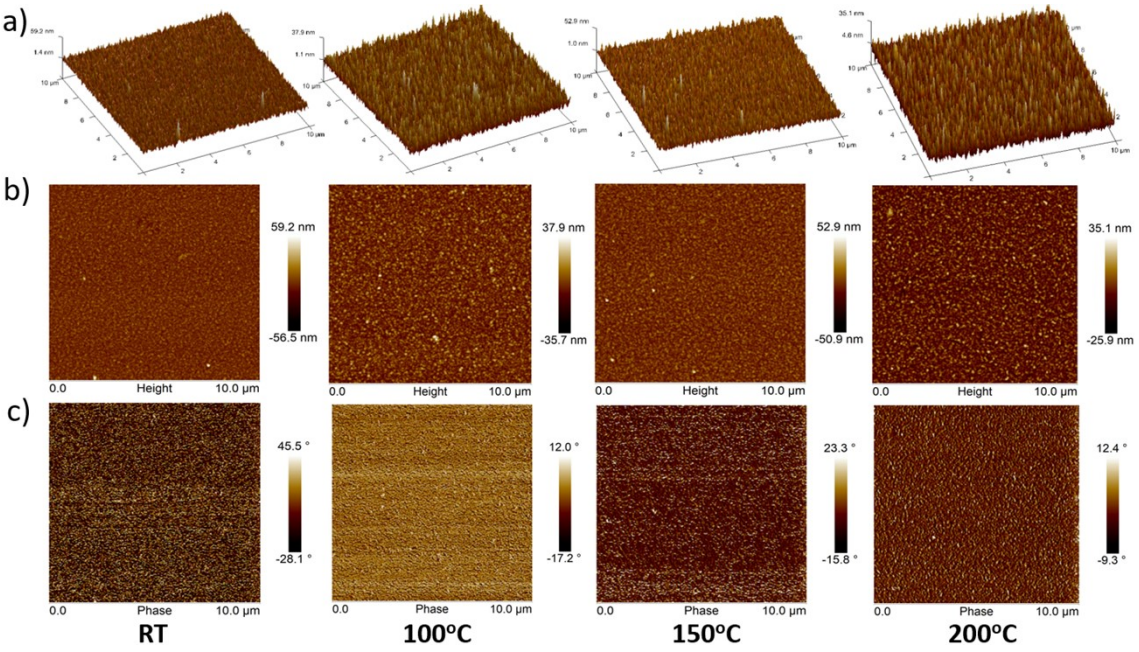

Figure S20. Tapping-mode AFM images of (a) 3D-topography, (b) height and (c) phase in 10 µm x 10 µm scan size of thin films of **P2** deposited on OTS-treated Si/SiO_2 substrates annealed at different temperatures.

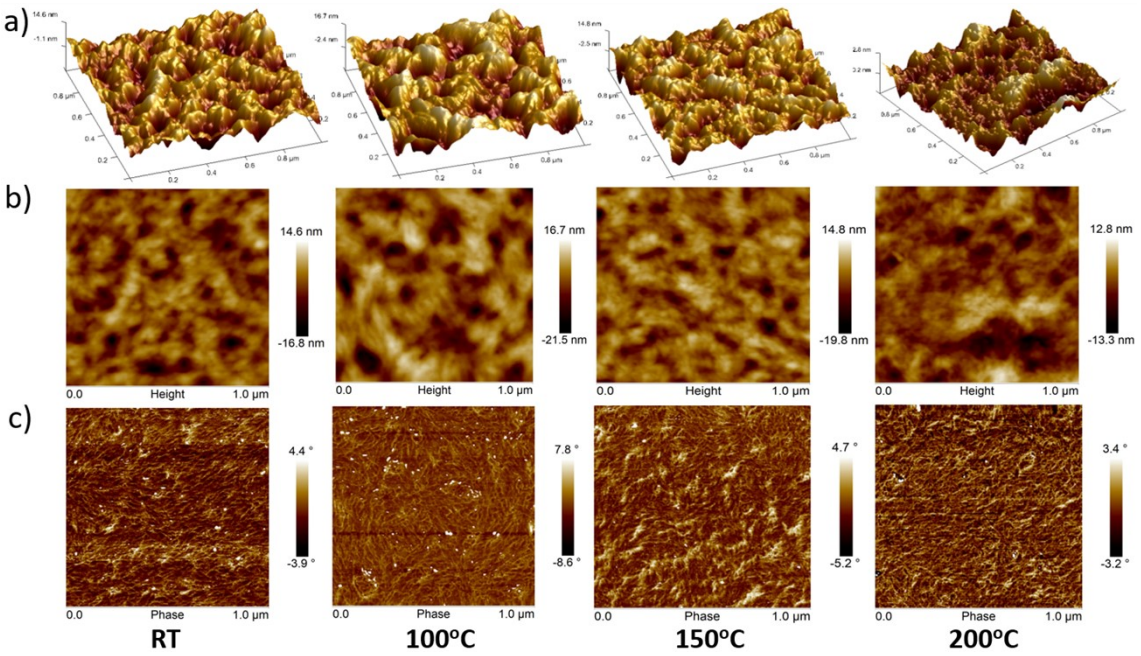

Figure S21. Tapping-mode AFM images of (a) 3D-topography, (b) height and (c) phase in 1 µm x 1 µm scan size of thin films of **P3** deposited on OTS-treated Si/SiO_2 substrates annealed at different temperatures.

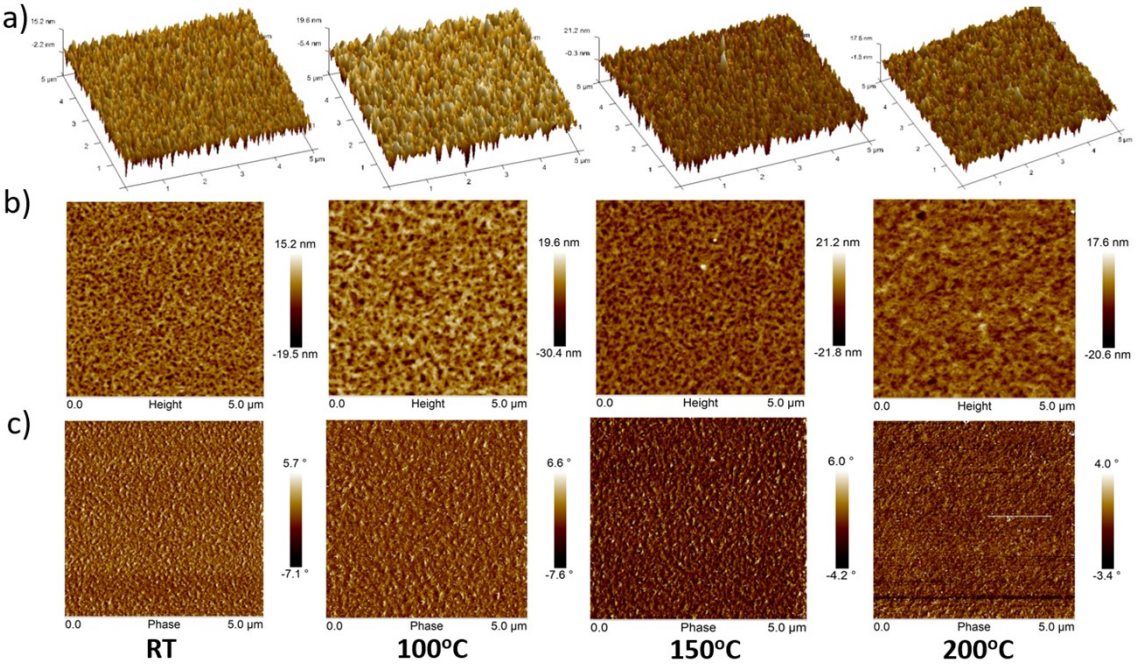

Figure S22. Tapping-mode AFM images of (a) 3D-topography, (b) height and (c) phase in 5 µm x 5 µm scan size of thin films of **P3** deposited on OTS-treated Si/SiO_2 substrates annealed at different temperatures.

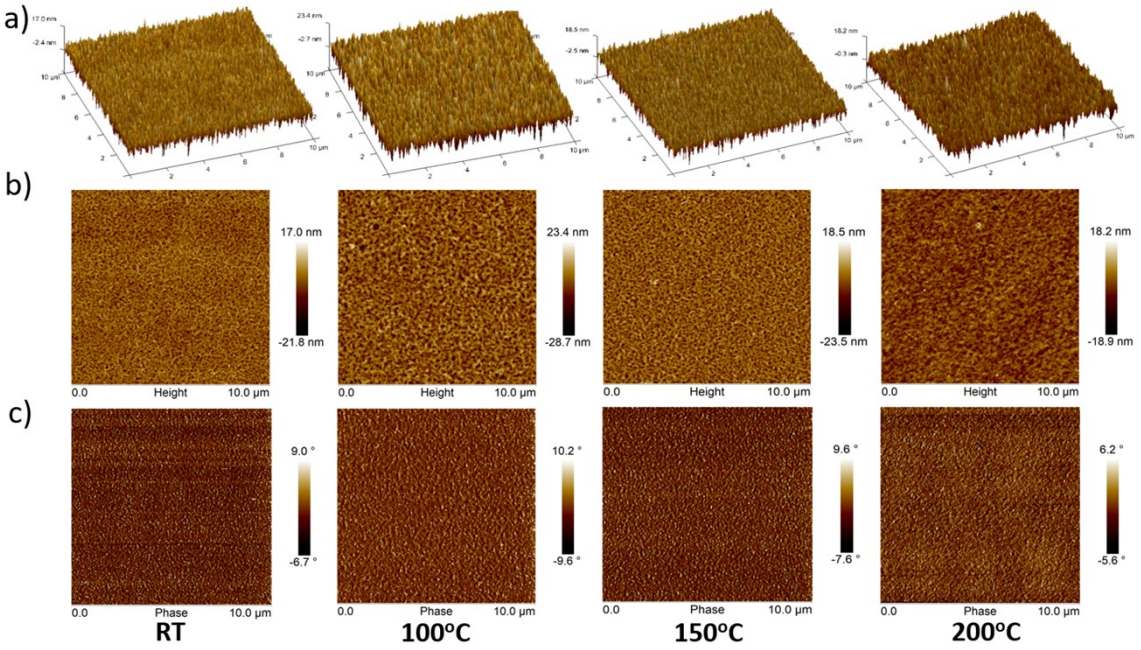

Figure S23. Tapping-mode AFM images of (a) 3D-topography, (b) height and (c) phase in 10 µm x 10 µm scan size of thin films of **P3** deposited on OTS-treated Si/SiO_2 substrates annealed at different temperatures.

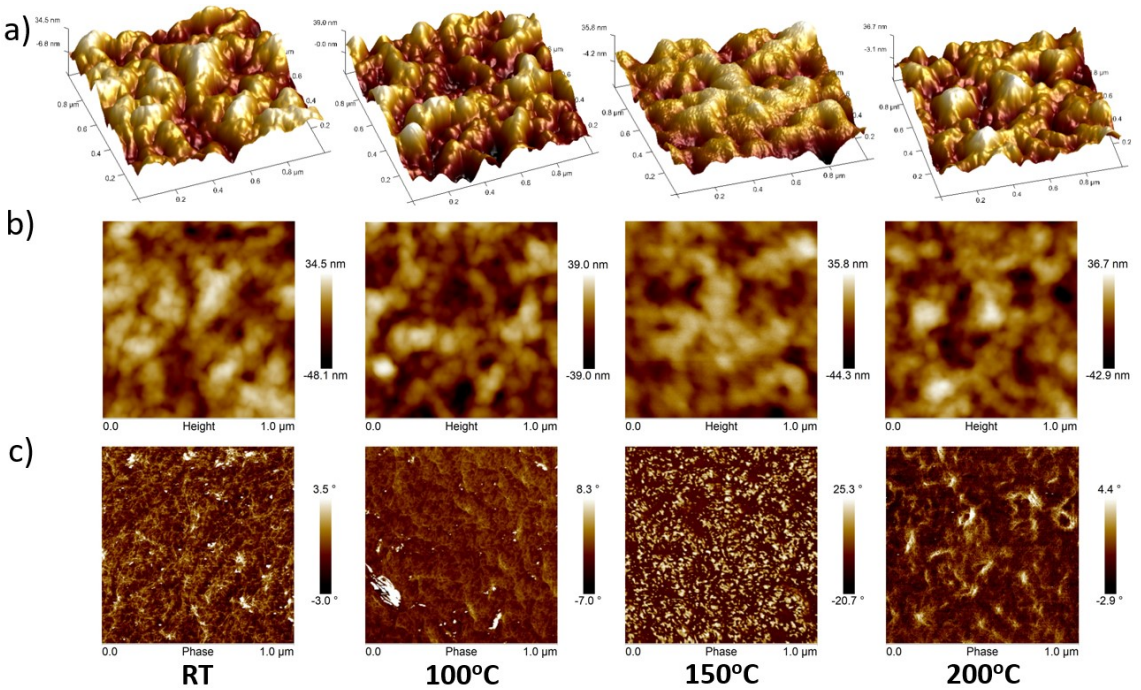

Figure S24. Tapping-mode AFM images of (a) 3D-topography, (b) height and (c) phase in 1 µm x 1 µm scan size of thin films of **P4** deposited on OTS-treated Si/SiO_2 substrates annealed at different temperatures.

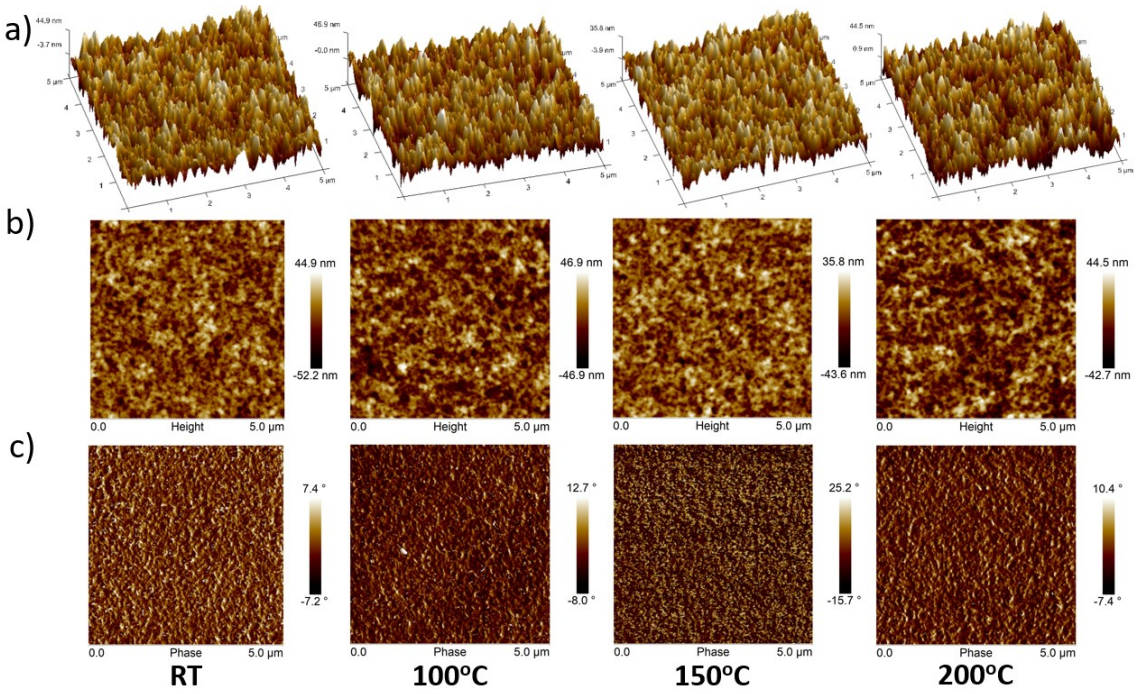

Figure S25. Tapping-mode AFM images of (a) 3D-topography, (b) height and (c) phase in 5 µm x 5 µm scan size of thin films of **P4** deposited on OTS-treated Si/SiO_2 substrates annealed at different temperatures.

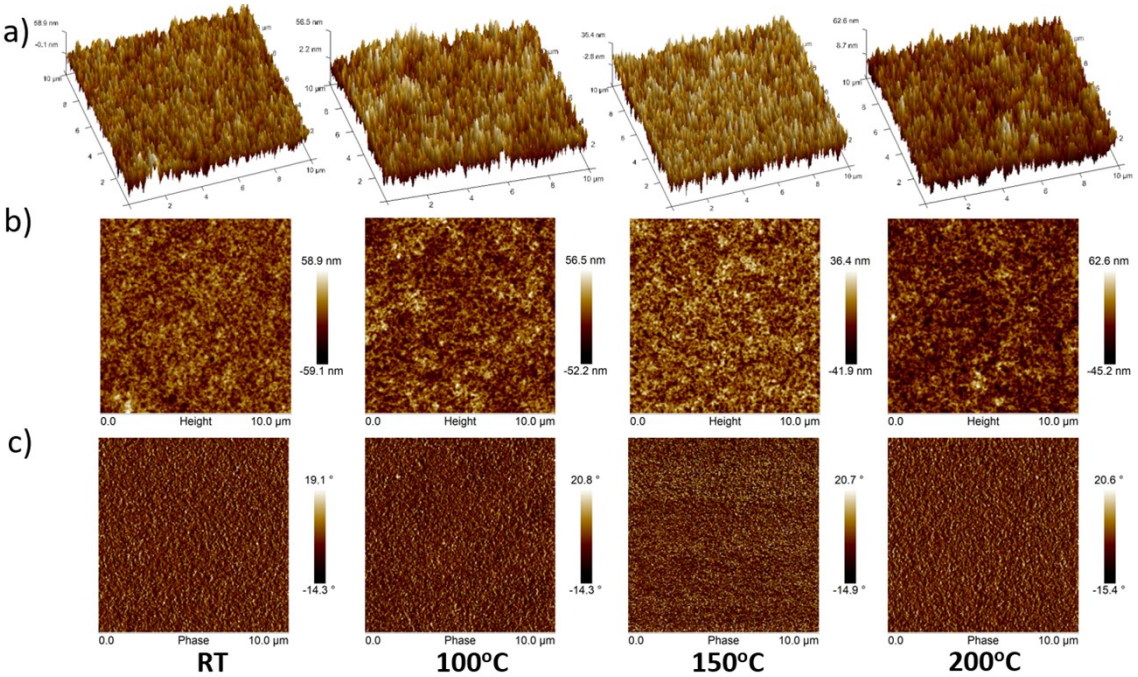

Figure S26. Tapping-mode AFM images of (a) 3D-topography, (b) height and (c) phase in 10 µm x 10 µm scan size of thin films of **P4** deposited on OTS-treated Si/SiO_2 substrates annealed at different temperatures.

7. Raman Spectroscopy

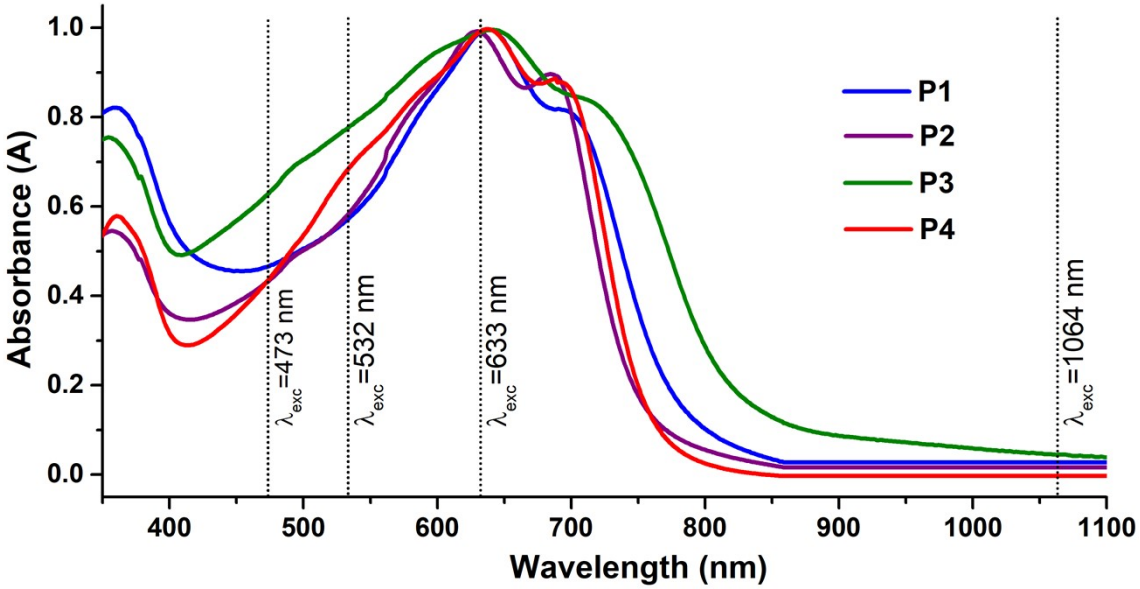

Figure S27. UV-Vis absorption spectra of the studied polymer thin films indicating the laser wavelengths used for resonance Raman studies.

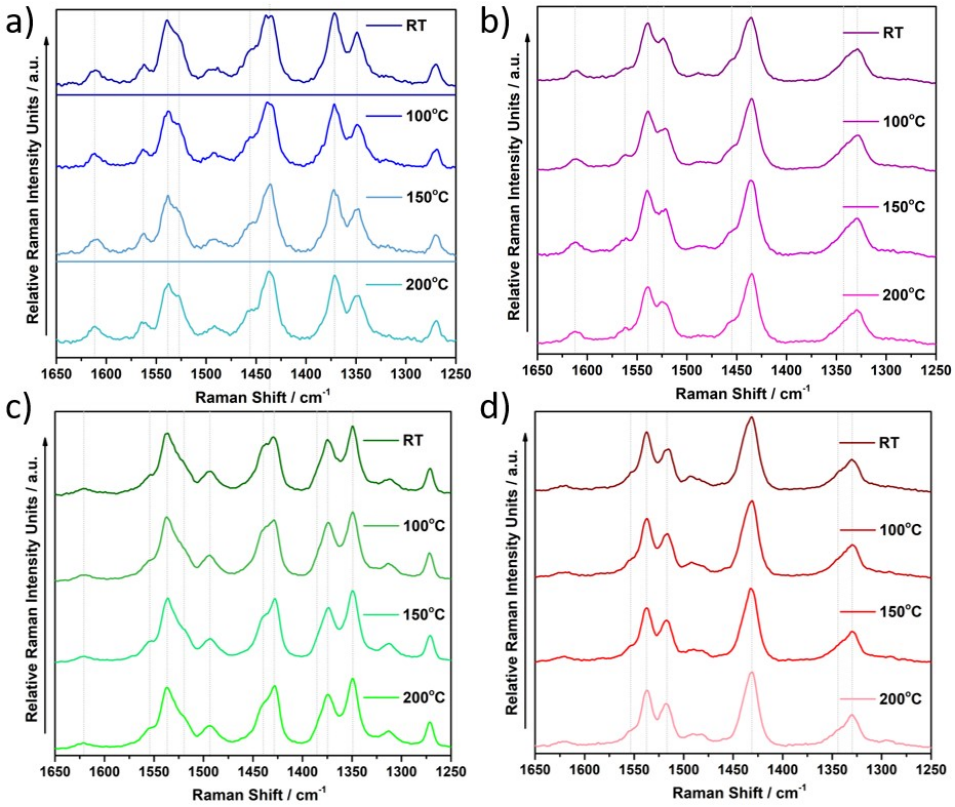

Figure S28. Resonance Raman spectra of annealed thin films of polymers **P1** (a), **P2** (b), **P3** (c) and **P4** (d) under 473 nm excitation.

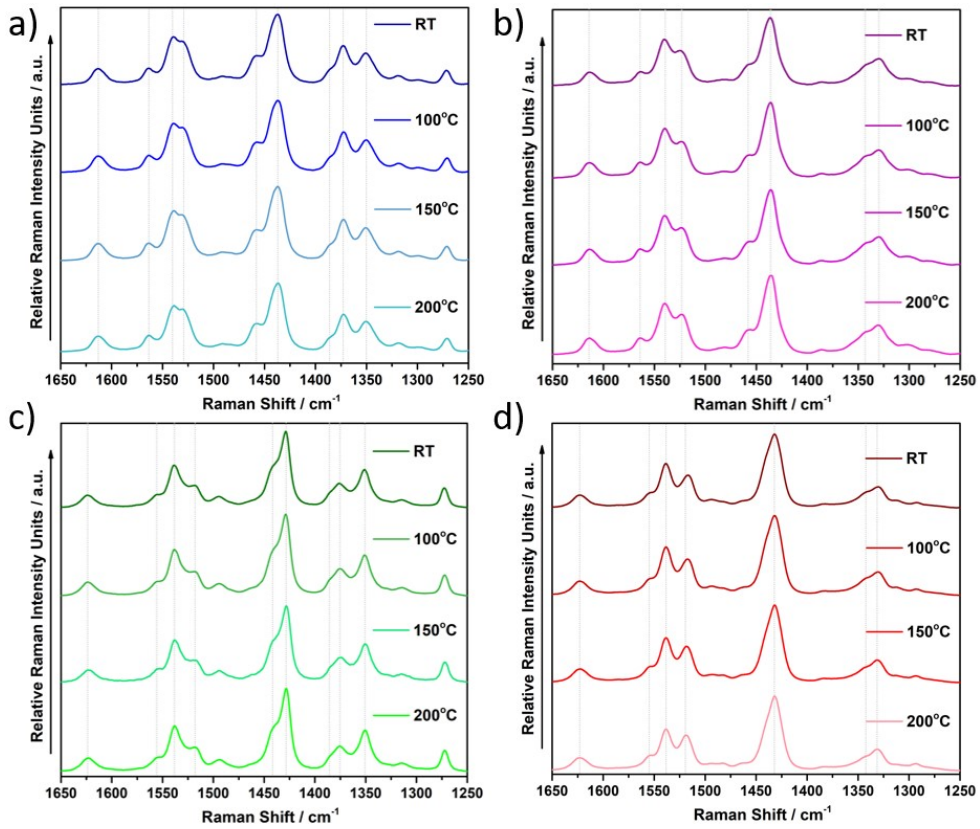

Figure S29. Resonance Raman spectra of annealed thin films of polymers **P1** (a), **P2** (b), **P3** (c) and **P4** (d) under 532 nm excitation.

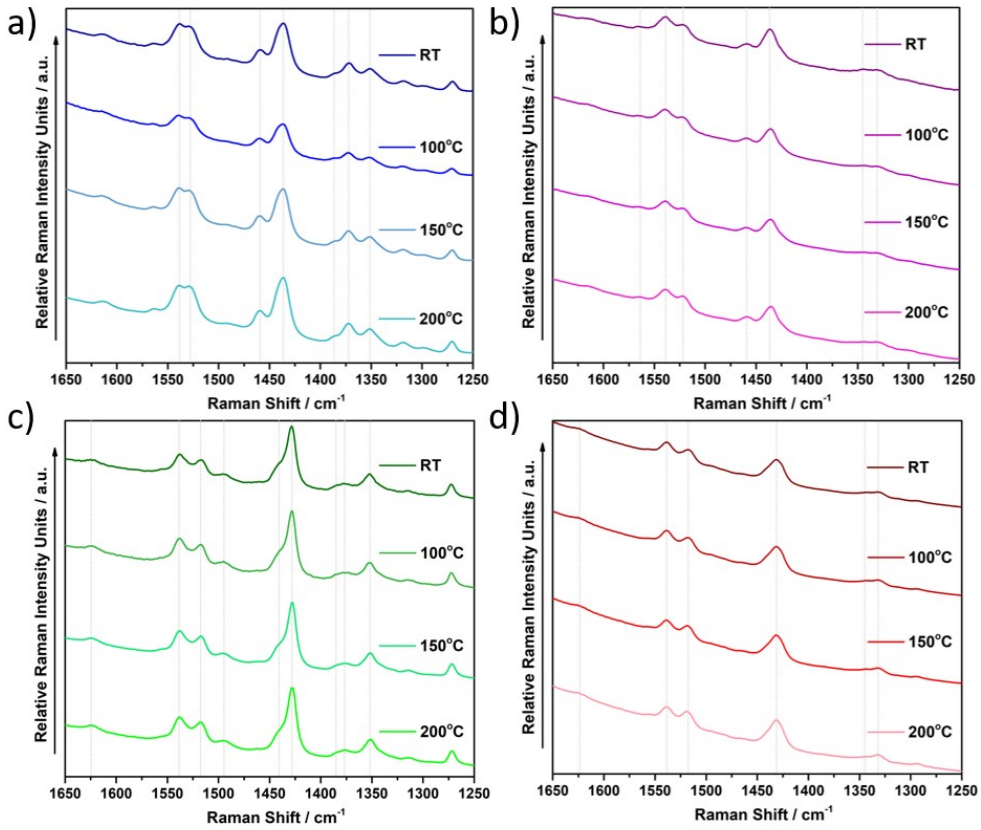

Figure S30. Resonance Raman spectra of annealed thin films of polymers **P1** (a), **P2** (b), **P3** (c) and **P4** (d) under 633 nm excitation.

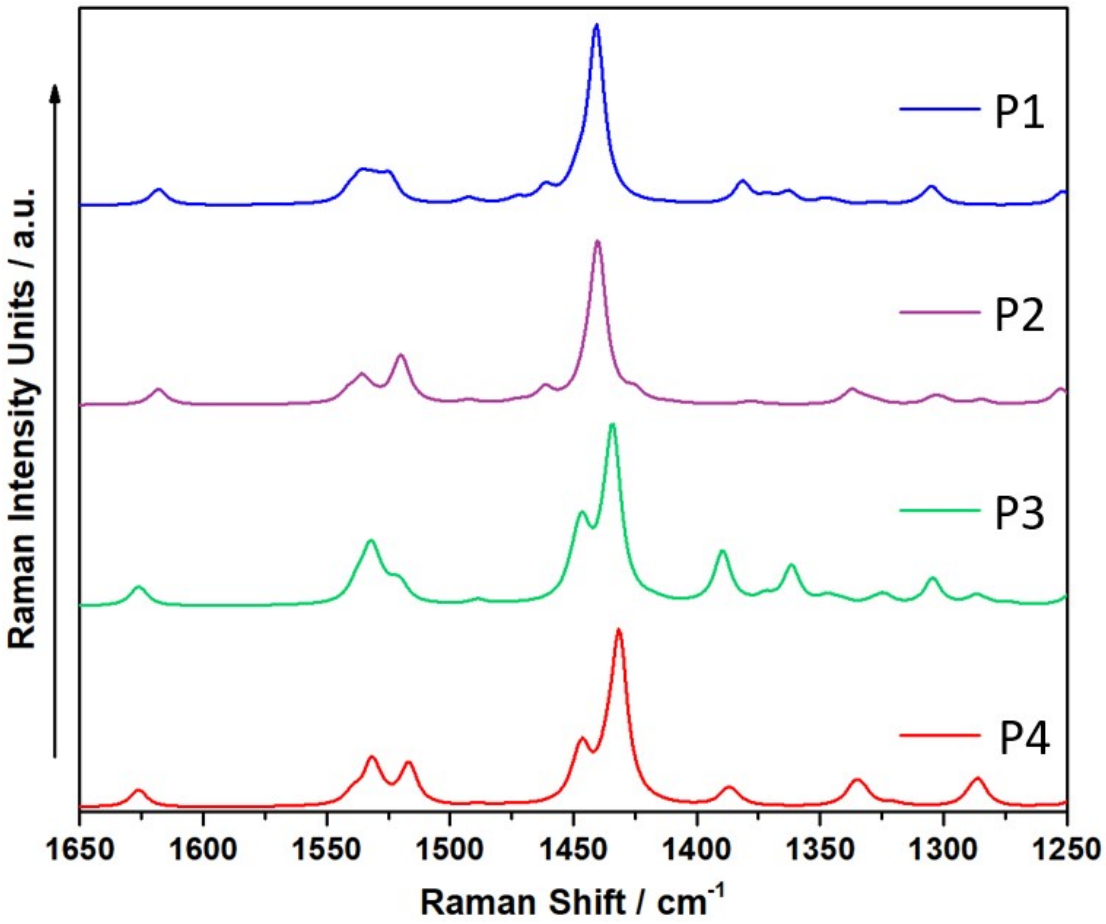

Figure S31. B3LYP/6-31G** Raman spectra for the dimeric models of **P1**, **P2**, **P3** and **P4** polymers.

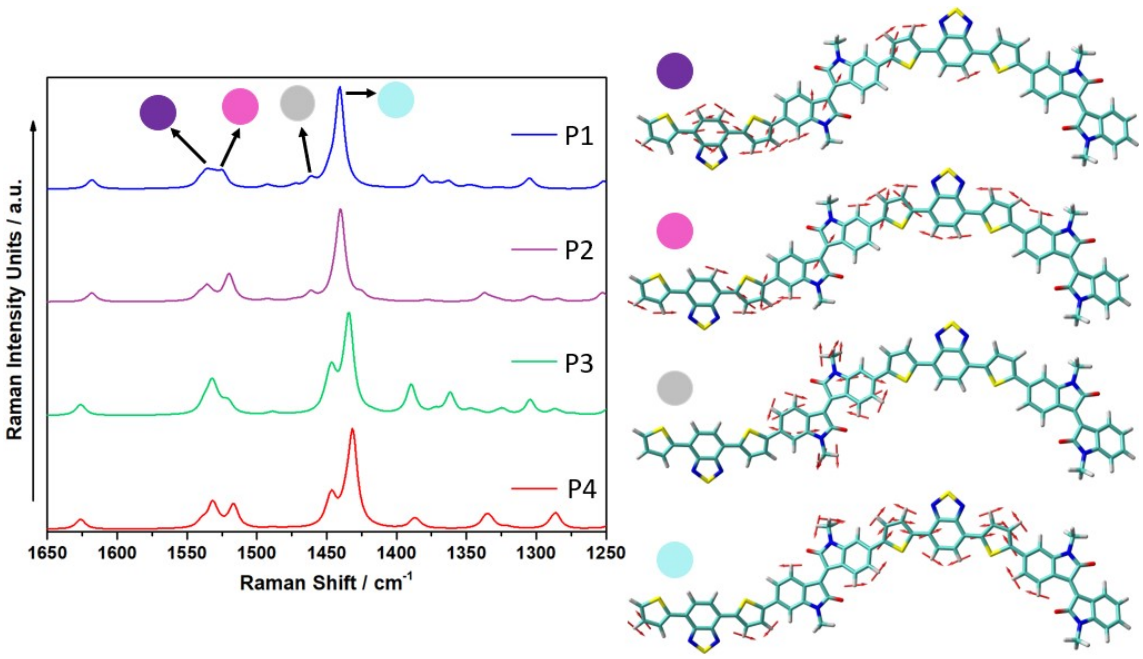

Figure S32. Theoretical Raman spectrum and vibrational eigenvectors associated with the most outstanding C=C/C-C Raman features for the dimeric models of **P1**, at B3LYP/6-31G** level.

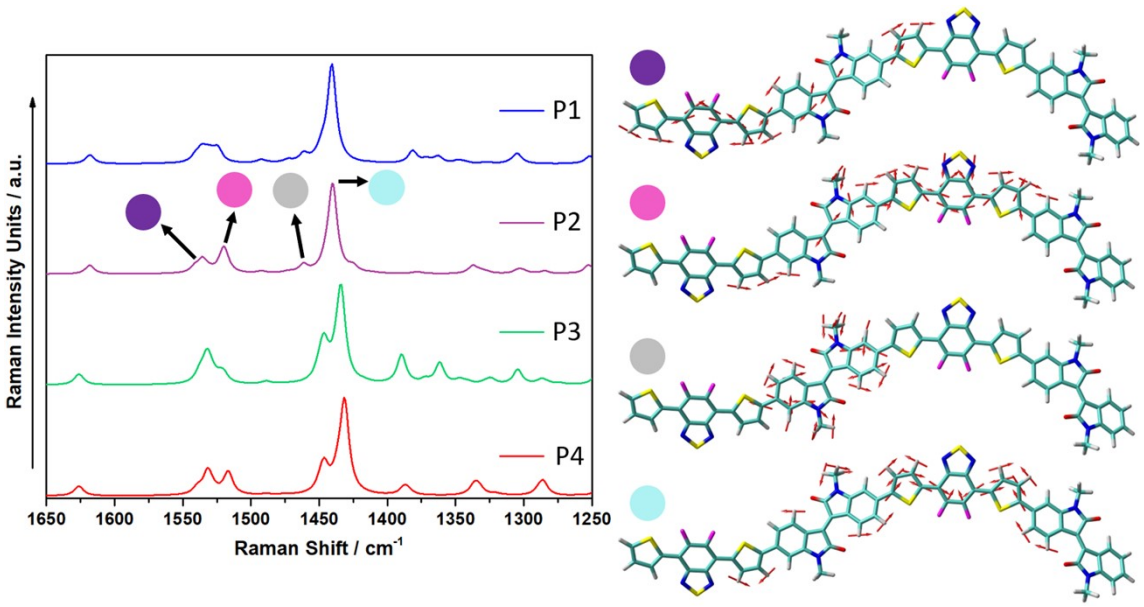

Figure S33. Theoretical Raman spectrum and vibrational eigenvectors associated with the most outstanding C=C/C-C Raman features for the dimeric models of **P2**, at B3LYP/6-31G** level.

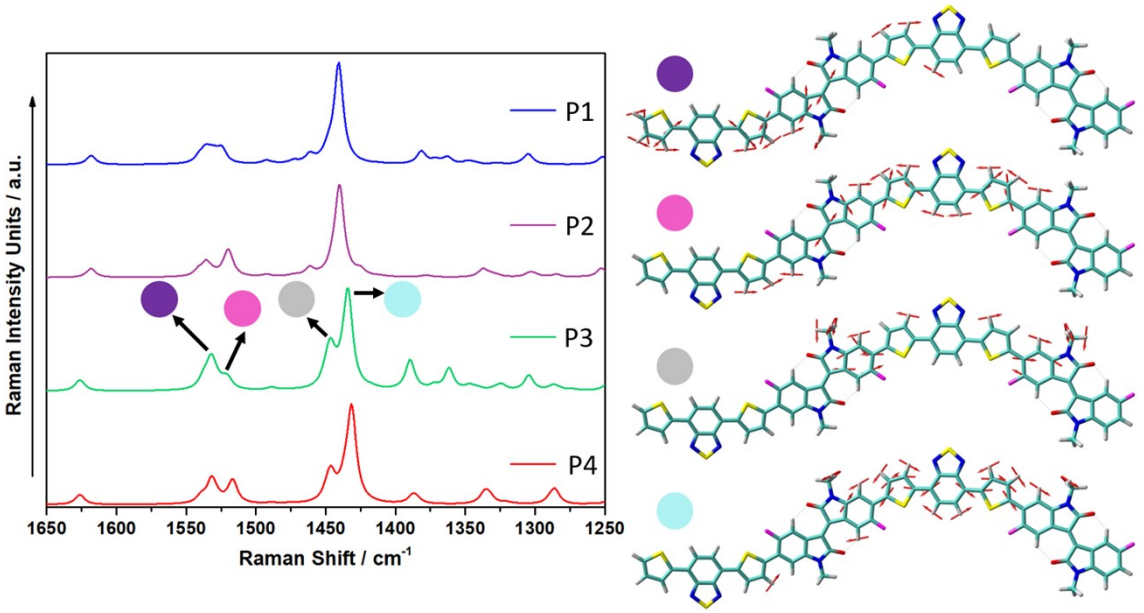

Figure S34. Theoretical Raman spectrum and vibrational eigenvectors associated with the most outstanding C=C/C-C Raman features for the dimeric models of **P3**, at B3LYP/6-31G** level.

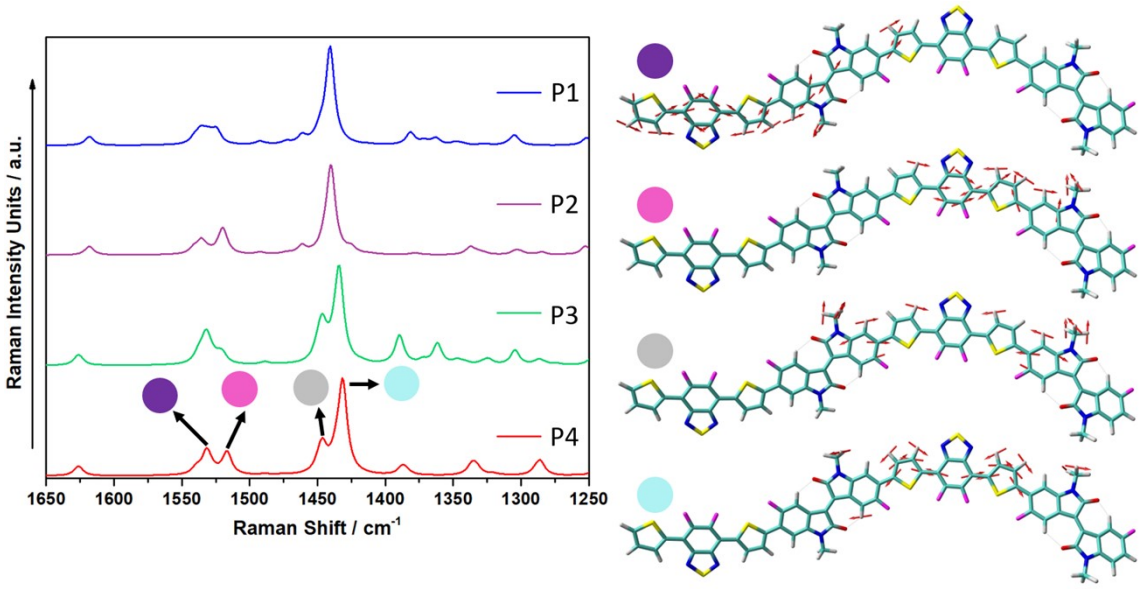

Figure S35. Theoretical Raman spectrum and vibrational eigenvectors associated with the most outstanding C=C/C-C Raman features for the dimeric models of **P4**, at B3LYP/6-31G** level.

8. References

1. (a) Lee, C.; Yang, W.; Parr, R. G., Development of the Colle-Salvetti correlation-energy formula into a functional of the electron density. *Phys. Rev. B* **1988,** *37* (2), 785-789; (b) Becke, A. D., Density-functional thermochemistry. III. The role of exact exchange. *J. Chem. Phys.* **1993,** *98* (7), 5648-5652.
2. Chai, J.-D.; Head-Gordon, M., Long-range corrected hybrid density functionals with damped atom–atom dispersion corrections. *Phys. Chem. Chem. Phys.* **2008,** *10* (44), 6615-6620.
3. (a) Hehre, W. J.; Ditchfield, R.; Pople, J. A., Self—Consistent Molecular Orbital Methods. XII. Further Extensions of Gaussian—Type Basis Sets for Use in Molecular Orbital Studies of Organic Molecules. *J. Chem. Phys.* **1972,** *56* (5), 2257-2261; (b) Francl, M. M.; Pietro, W. J.; Hehre, W. J.; Binkley, J. S.; Gordon, M. S.; DeFrees, D. J.; Pople, J. A., Self-consistent molecular orbital methods. XXIII. A polarization-type basis set for second-row elements. *J. Chem. Phys.* **1982,** *77* (7), 3654-3665.
4. M. J. Frisch, G. W. T., H. B. Schlegel, G. E. Scuseria, M. A. Robb, J. R. Cheeseman, G. Scalmani, V. Barone, G. A. Petersson, H. Nakatsuji, X. Li, M. Caricato, A. V. Marenich, J. Bloino, B. G. Janesko, R. Gomperts, B. Mennucci, H. P. Hratchian, J. V. Ortiz, A. F. Izmaylov, J. L. Sonnenberg, D. Williams-Young, F. Ding, F. Lipparini, F. Egidi, J. Goings, B. Peng, A. Petrone, T. Henderson, D. Ranasinghe, V. G. Zakrzewski, J. Gao, N. Rega, G. Zheng, W. Liang, M. Hada, M. Ehara, K. Toyota, R. Fukuda, J. Hasegawa, M. Ishida, T. Nakajima, Y. Honda, O. Kitao, H. Nakai, T. Vreven, K. Throssell, J. A. Montgomery, Jr., J. E. Peralta, F. Ogliaro, M. J. Bearpark, J. J. Heyd, E. N. Brothers, K. N. Kudin, V. N. Staroverov, T. A. Keith, R. Kobayashi, J. Normand, K. Raghavachari, A. P. Rendell, J. C. Burant, S. S. Iyengar, J. Tomasi, M. Cossi, J. M. Millam, M. Klene, C. Adamo, R. Cammi, J. W. Ochterski, R. L. Martin, K. Morokuma, O. Farkas, J. B. Foresman, and D. J. Fox. , Gaussian 16, Revision B.01. *Gaussian, Inc., Wallingford CT,* **2016**.
5. https://www.chemcraftprog.com, Chemcraft - graphical software for visualization of quantum chemistry computations. .

6. (a) Runge, E.; Gross, E. K. U., Density-Functional Theory for Time-Dependent Systems. *Phys. Rev. Lett.* **1984,** *52* (12), 997-1000; (b) Gross, E. K. U.; Kohn, W., Time-Dependent Density-Functional Theory. In *Advances in Quantum Chemistry*, Löwdin, P.-O., Ed. Academic Press: 1990; Vol. 21, pp 255-291; (c) Gross, E.; Ullrich, C.; Gossmann, U. In *In Density Functional Theory; Gross, EKU; Dreizler, RM, Eds*, NATO Advanced Study Institute Series B: Physics, 1995; pp 149-171.